The Astrophysical Journal, 945:107 (15pp), 2023 March 10 https://doi.org/10.3847/1538-4357/acb8a9

Circumstellar Medium Interaction in SN 2018lab, A Low-luminosity Type IIP Supernova Observed with TESS

Jeniveve Pearson[1], Griffin Hosseinzadeh[1], David J. Sand[1], Jennifer E. Andrews[2], Jacob E. Jencson[1], Yize Dong (董一泽)[3], K. Azalee Bostroem[4], S. Valenti[3], Daryl Janzen[5], Nicolás Meza Retamal[3], M. J. Lundquist[6], Samuel Wyatt[1], R. C. Amaro[1], Jamison Burke[7,8], D. Andrew Howell[7,8], Curtis McCully[7,8], Daichi Hiramatsu[9,10], Saurabh W. Jha[11], Nathan Smith[1], Joshua Haislip[12], Vladimir Kouprianov[12], Daniel E. Reichart[12], Yi Yang[13], and Jeonghee Rho[14]

[1] Steward Observatory, University of Arizona, 933 North Cherry Avenue, Tucson, AZ, 85721-0065, USA; jenivevepearson@arizona.edu
[2] Gemini Observatory, 670 North A'ohoku Place, Hilo, HI, 96720-2700, USA
[3] Department of Physics and Astronomy, University of California, Davis, 1 Shields Avenue, Davis, CA, 95616-5270, USA
[4] Department of Astronomy, University of Washington, 3910 15th Avenue NE, Seattle, WA, 98195-0002, USA
[5] Department of Physics & Engineering Physics, University of Saskatchewan, 116 Science Place, Saskatoon, SK, S7N 5E2, Canada
[6] W. M. Keck Observatory, 65-1120 Māmalahoa Highway, Kamuela, HI, 96743-8431, USA
[7] Las Cumbres Observatory, 6740 Cortona Drive, Suite 102, Goleta, CA, 93117-5575, USA
[8] Department of Physics, University of California, Santa Barbara, CA, 93106-9530, USA
[9] Center for Astrophysics | Harvard & Smithsonian, 60 Garden Street, Cambridge, MA, 02138-1516, USA
[10] The NSF AI Institute for Artificial Intelligence and Fundamental Interactions, USA
[11] Department of Physics and Astronomy, Rutgers, the State University of New Jersey, 136 Frelinghuysen Road, Piscataway, NJ, 08854-8019, USA
[12] Department of Physics and Astronomy, University of North Carolina, 120 East Cameron Avenue, Chapel Hill, NC, 27599, USA
[13] Department of Astronomy, University of California, Berkeley, CA, 94720-3411, USA
[14] SETI Institute, 339 Bernardo Ave, Suite 200, Mountain View, CA, 94043, USA
Received 2022 August 30; revised 2023 January 28; accepted 2023 February 1; published 2023 March 13

Abstract

We present photometric and spectroscopic data of SN 2018lab, a low-luminosity Type IIP supernova (LLSN) with a V-band peak luminosity of -15.1 ± 0.1 mag. SN 2018lab was discovered by the Distance Less Than 40 Mpc (DLT40) SN survey only 0.73 days post-explosion, as determined by observations from the Transiting Exoplanet Survey Satellite (TESS). TESS observations of SN 2018lab yield a densely sampled, fast-rising, early-time light curve likely powered by ejecta–circumstellar medium (CSM) interaction. The blueshifted, broadened flash feature in the earliest spectra (<2 days) of SN 2018lab provides further evidence for ejecta–CSM interaction. The early emission features in the spectra of SN 2018lab are well described by models of a red supergiant progenitor with an extended envelope and a close-in CSM. As one of the few LLSNe with observed flash features, SN 2018lab highlights the need for more early spectra to explain the diversity of the flash feature morphology of Type II SNe.

Unified Astronomy Thesaurus concepts: Supernovae (1668); Core-collapse supernovae (304); Type II supernovae (1731); Circumstellar matter (241)

Supporting material: data behind figures

1. Introduction

Type IIP/IIL supernovae (SNe II) are the result of core collapse (CC) in stars $>8\ M_{\odot}$, and are defined by the appearance of hydrogen in their spectra (Filippenko 1997; Smartt et al. 2009). SNe II have proven to be a continuous population smoothly spanning significant photometric, $-19.0 \lesssim M_V \lesssim -13.0$ mag at peak, and spectroscopic diversities (Anderson et al. 2014; Sanders et al. 2015; Valenti et al. 2016; Gutiérrez et al. 2017). The extrema of the SNe II distribution have been the subject of intense study. SNe II with peak magnitudes $M_V \gtrsim -15.5$ are referred to as low-luminosity (LL) SNe (Pastorello et al. 2004). The plateau luminosities of SNe II correlate with their photospheric expansion velocities (Hamuy & Pinto 2002; Pejcha & Prieto 2015). In line with this relation, LLSNe have the lowest expansion speeds ($\sim$1300–2500 km s^{-1} at 50 days post-explosion; Pastorello et al. 2004; Spiro et al. 2014) of all SNe II. LLSNe also have smaller ejecta kinetic energies ($\sim$0.1–0.5 $\times 10^{51}$ erg; Pumo et al. 2017) and lower nickel masses ($\leqslant 10^{-2}\ M_{\odot}$; Turatto et al. 1998; Pastorello et al. 2004; Spiro et al. 2014) than typical SNe II (Pastorello et al. 2004).

The progenitors of LLSNe are unclear, despite their similarities to more-luminous SNe II. The controversy surrounding the progenitors of LLSNe began with the discovery and subsequent progenitor modeling of SN 1997D (Turatto et al. 1998; Benetti et al. 2001). The characteristics of SN 1997D were well explained by models of both the CC of a $>20\ M_{\odot}$ star with a large amount of fallback (Turatto et al. 1998; Zampieri et al. 1998) and of a star near the mass limit for undergoing CC (8–10 $M_{\odot}$; Chugai & Utrobin 2000). In the time since, studies have supported both high- (Zampieri et al. 2003; $>20\ M_{\odot}$) and low-mass (Pignata 2013; Lisakov et al. 2017, 2018; Pumo et al. 2017; Kozyreva et al. 2022; 8–10 $M_{\odot}$) red supergiant (RSG) progenitor models. Models with less massive (8–10 $M_{\odot}$) progenitors have become popular in recent years as archival pre-explosion Hubble Space Telescope (HST) images have placed upper limits on the progenitor masses of numerous LLSNe (Van Dyk et al. 2003, 2012; Maund & Smartt 2005; Li et al. 2006; Smartt et al. 2009; Fraser et al. 2011; Maund et al. 2014).

Electron-capture (EC) SNe, the result of O-Ne-Mg CC in super-asymptotic giant branch (AGB) stars, have also been used to explain the properties of some LLSNe (Hosseinzadeh et al. 2018; Valerin et al. 2022). Some models predict that ECSNe can appear nearly identical to LL-CCSNe (Nomoto 1984; Kitaura et al. 2006; Poelarends et al. 2008) and their progenitors lie in the same mass range (super-AGB stars 8–10 $M_{\odot}$; Kitaura et al. 2006) as low-mass RSGs which undergo CC. Reliably distinguishing between the ECSN and LL-CCSN populations remains a challenge (Zhang et al. 2020; Callis et al. 2021; Hiramatsu et al. 2021b).

All massive stars are expected to lose mass, however the properties of mass loss (e.g., density, radial extent, physical location) vary for different progenitors (Smith 2014). Therefore, the extent of ejecta–CSM interaction is a possible indicator of whether an LLSN is from EC or CC. Super-AGB stars readily produce large CSM envelopes as a result of their thermal pulsation phase. RSGs often have a nearby CSM as well, though often much less than super-AGB stars, due to late-stage episodic and eruptive mass loss. Indicators of ejecta–CSM interaction are sometimes only visible in the hours and days immediately following an SN explosion, before the SN ejecta has completely overtaken any CSM. Ejecta–CSM interaction can result in increased luminosity within the first weeks following explosion, observed as a bump or fast rise in the early light curve (Anderson et al. 2014; González-Gaitán et al. 2015; Valenti et al. 2016; Morozova et al. 2017, 2018; Förster et al. 2018; Hiramatsu et al. 2021a). A more dense and substantial CSM will result in a larger—and possibly longer—excess luminosity, and have a greater effect on the early light curve. LLSNe with pronounced early-time light-curve bumps, like SN 2016bkv (Hosseinzadeh et al. 2018), may have super-AGB progenitors.

Narrow emission lines observed in the spectra of SNe in the days following explosion can be used to indicate the composition, density, and velocity of the CSM surrounding the progenitor (Gal-Yam et al. 2014). These narrow lines, often referred to as "flash" spectroscopy, are the result of recombination of the CSM ionized by the shock-breakout flash (Khazov et al. 2016) or very early ejecta–CSM interaction (Shivvers et al. 2015; Smith et al. 2015), which ends when the CSM is entirely swept up by the expanding ejecta.

Narrow lines from ionized CSM have been detected in the hours following explosion in some instances (Niemela et al. 1985; Benetti et al. 1994; Quimby et al. 2007; Gal-Yam et al. 2014). When these spectral features are detected, they can provide insight into the composition and mass-loss history of the progenitor (Groh et al. 2014; Yaron et al. 2017; Davies & Dessart 2019). To date the only LLSN that clearly exhibits narrow early-time flash features is SN 2016bkv (Hosseinzadeh et al. 2018).

A few SNe have shown signs of broadened, blueshifted features rather than narrow ones in the days following explosion (Soumagnac et al. 2020; Bruch et al. 2021; Hosseinzadeh et al. 2022). These broad features, hereafter referred to as broad-lined flash features, are produced when the outer layers of the SN ejecta interact with a low-density CSM. The substantial CSM surrounding a super-AGB progenitor is likely to produce narrow lines at ∼5 days which can persist for up to a week, whereas a CSM surrounding an RSG progenitor produces flash features which are typically expected to broaden and fade by ∼5 days post-explosion (Hiramatsu et al. 2021b).

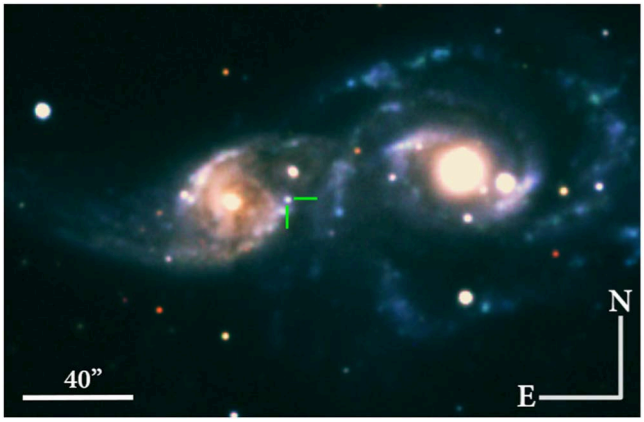

Figure 1. Composite *g*, *r*, *i* image of SN 2018lab (indicated by the green tick marks) in IC 2163 (left) obtained by the Las Cumbres Observatory on 2019 January 10. NGC 2207 is on the right.

We must emphasize that the prolonged existence of narrow-lined flash features in and of itself does not distinguish super-AGB progenitors from RSG progenitors. Some SNe with RSG progenitors exhibit narrow-lined flash features that remain visible for over a week (SN 1998S; Leonard et al. 2000; Fassia et al. 2001; SN 2020tlf; Jacobson-Galán et al. 2022) and while the suggested ECSN SN 2018zd has long-lived narrow-lined flash features (Hiramatsu et al. 2021b), SN 2018zd might be a CCSN with an RSG progenitor (Zhang et al. 2020; Callis et al. 2021). However, no LLSN with narrow-lined flash features has a confirmed RSG progenitor. So in LLSNe, short-lived, early-time, broadened, blueshifted flash features could be an indicator of an RSG progenitor rather than a super-AGB one, assuming there is no extreme long-term mass loss around the RSG.

In this work, we present spectroscopic and photometric data for SN 2018lab, an LLSN which displays clear signs of CSM interaction: a fast-rising light curve and a broad-lined flash feature in the early spectra (<2 days). In Section 2 the discovery and classification of SN 2018lab is reviewed. In Section 3 the observations and data reduction are outlined. In Section 4 the photometric evolution is discussed. In Section 5 we present the spectroscopic evolution. These results are summarized in Section 6.

2. Discovery and Classification

SN 2018lab, also known as DLT18ar, was first discovered, at R.A.(2000) = $06^{h}16^{m}26\overset{s}{.}520$ and decl.(2000) = $-21^{\circ}22'32\overset{''}{.}38$, by the Distance Less Than 40 Mpc Survey (DLT40; for survey details see Tartaglia et al. 2018) on 2018 December 29 at 03:01:26 UTC (58481.126 MJD; Sand et al. 2018).

The redshift of SN 2018lab is $z_{18lab} = 0.0089$, measured using the host Hα in the first spectrum (1.6 days after explosion). SN 2018lab is located between the interacting galaxies IC 2163 and NGC 2207 (see Figure 1). IC 2163 and NGC 2207 are a well-studied pair of interacting, grazing galaxies (Elmegreen et al. 1995a, 1995b, 2001, 2006; Struck et al. 2005) that frequently produce SNe, notably SN 1975A (Kirshner et al. 1976; Arnett 1982), SN 2003H (Filippenko et al. 2003; Lyman et al. 2014), SN 2010jp (Smith et al. 2012; Corgan et al. 2022), SN 2013ai (Davis et al. 2021), and SPIRITS 14buu, 15c, and 17lb (Jencson et al. 2017, 2019). IC 2163 has a redshift $z = 0.0090$ (de Vaucouleurs et al. 1991) and

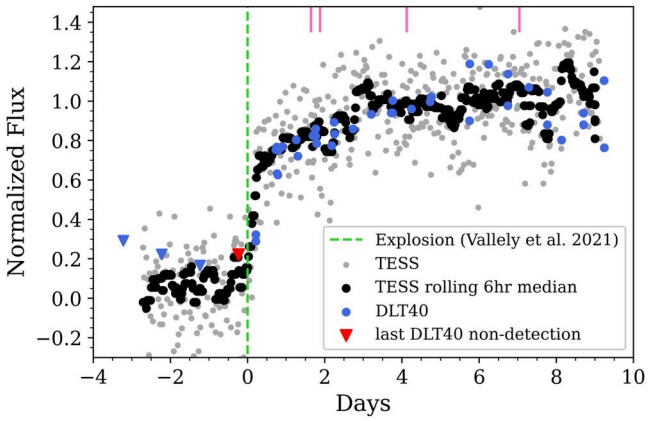

Figure 2. TESS band SN 2018lab light curve (gray and black) and *r*-band corrected DLT40 (blue and red) data. The times of the spectral epochs are marked in pink ticks at the top. The explosion time as reported in Vallely et al. (2021) is marked by the green dashed line. This value is extremely well constrained by both the TESS and DLT40 observations (see Figure 3 for a zoomed-in version). The light curves are normalized to the median value of the data 3–8 days after explosion.

NGC 2207 has a redshift $z = 0.0092$ (Springob et al. 2005). The measured redshift to SN 2018lab is most consistent with that of IC 2163, which is quoted as the host galaxy throughout this work.

IC 2163 was in the Transiting Exoplanet Survey Satellite (TESS; Ricker et al. 2015) footprint when SN 2018lab exploded. TESS observations of SN 2018lab yield an explosion date of MJD 58480.4 ± 0.1, as published in Vallely et al. (2021), see their Equation (2) and Table 1. This explosion time is 0.24 days after the last DLT40 non-detection and 0.73 days before DLT40's discovery of SN 2018lab, as seen in Figure 2. We adopt the TESS-derived explosion epoch throughout this work. Spectroscopic classification done on 2018 December 31 at 06:42:29 UTC, 2 days after the explosion, confirmed that the object was an SN II (Razza et al. 2018).

3. Observations and Data Reduction

3.1. Follow-up Photometry and Spectroscopy

3.1.1. Photometry

SN 2018lab was observed by TESS during the mission's Sector 6 operations, from 2018 December 15 18:36:03.542 to 2019 January 6 12:36:19.181 UTC. The TESS light curve of SN 2018lab was previously published in Vallely et al. (2021). In Figure 2, the TESS photometry, both unbinned and rolling 6 hr medians, is plotted.

Following the discovery of SN 2018lab by the DLT40 survey, continued monitoring was done by two of DLT40's discovery telescopes, the PROMPT5 0.4 m telescope at the Cerro Tololo Inter-American Observatory and the PROMPT-MO 0.4 m telescope at the Meckering Observatory in Australia. Observations taken by these telescopes are calibrated to the Sloan Digital Sky Survey (SDSS) *r* band, as described in Tartaglia et al. (2018), and are shown in Figure 2.

Additional *UBVgri* photometry of SN 2018lab was obtained using the Sinistro cameras on Las Cumbres Observatory's robotic 1 m telescopes (Brown et al. 2013), located at the Siding Spring Observatory, the South African Astronomical Observatory, and the Cerro Tololo Inter-American Observatory. These are shown in Figure 3.

The photometric data from Las Cumbres Observatory was reduced using `lcogtsnpipe` (Valenti et al. 2016), a PyRAF-based image reduction pipeline. Given the complexity of the host, *UBVgri* reference images were obtained with Las Cumbres Observatory on 2021 August 25, >900 days after explosion, when the SN was no longer bright enough to be detectable. These reference frames were subtracted from the science images. Aperture photometry was then extracted from the difference images using `lcogtsnpipe`. Apparent magnitudes were calibrated to the APASS (*BVgri*) catalog and Landolt (*U*) standard fields observed on the same nights with the same telescopes.

Infrared photometry of SN 2018lab was also obtained with images from the Infrared Array Camera (IRAC; Fazio et al. 2004) on board the Spitzer Space Telescope (Werner et al. 2004; Gehrz et al. 2007). The host system was imaged several times between 2014 and 2019 in the IRAC1 (3.6 μm) and IRAC2 (4.5 μm) imaging bands by the SPitzer InfraRed Intensive Transients Survey (SPIRITS; PI M. Kasliwal; PIDs 10136, 11063, 13053, and 14089). The "postbasic calibrated data"-level images were downloaded from the Spitzer Heritage Archive[15] and processed through an automated image subtraction pipeline (for survey and pipeline details, see Kasliwal et al. 2017; Jencson et al. 2019). For reference images, we used the Super Mosaics,[16] consisting of stacks of images obtained on 2005 February 2. Aperture photometry was performed on the difference images adopting the appropriate aperture corrections and Vega-system zero-point fluxes from the IRAC instrument handbook[17] and following the method for a robust estimate of the photometric uncertainties as described in Jencson (2020). These data are presented in Figure 3.

3.1.2. Spectroscopy

We present 12 optical spectra of SN 2018lab ranging from less than 48 hr to over 300 days after explosion. Of the 12 spectra presented in this work, 11 were obtained as a result of a high-cadence spectroscopic follow-up campaign using the Robert Stobie Spectrograph (RSS) on the Southern African Large Telescope (SALT; Smith et al. 2006) using a 1.″50 slit width, the FLOYDS instruments (Brown et al. 2013) on the Las Cumbres Observatory's 2 m Faulkes Telescopes North and South (FTN/FTS) with the setup described in Brown et al. (2013) with a 2″ slit width, the Low Resolution Imaging Spectrometer (LRIS; Oke et al. 1995) on Keck I using a 1.″5 slit width, and one of the Multi-Object Double Spectrographs (MODS1; Pogge et al. 2010) on the LBT in the 1.″0 segmented longslit configuration. The LBT spectrum from 308 days post-explosion is discussed in Section 5.4. We also include in our analysis the classification spectrum from 1.9 days post-explosion (Razza et al. 2018) taken as part of the Public European Southern Observatory (ESO) Spectroscopic Survey for Transient Objects (ePESSTO; Smartt et al. 2015) using the ESO Faint Object Spectrograph and Camera (EF0SC2) on the ESO New Technology Telescope (ESO-NTT) using a 1″ slit width with the Grism#13 described in Smartt et al. (2015). All spectra are logged in Table 1.

[15] https://sha.ipac.caltech.edu/applications/Spitzer/SHA/

[16] Super Mosaics are available as Spitzer Enhanced Imaging Products through the NASA/IPAC Infrared Science Archive: https://irsa.ipac.caltech.edu/data/SPITZER/Enhanced/SEIP/overview.html.

[17] http://irsa.ipac.caltech.edu/data/SPITZER/docs/irac/iracinstrumenthandbook/

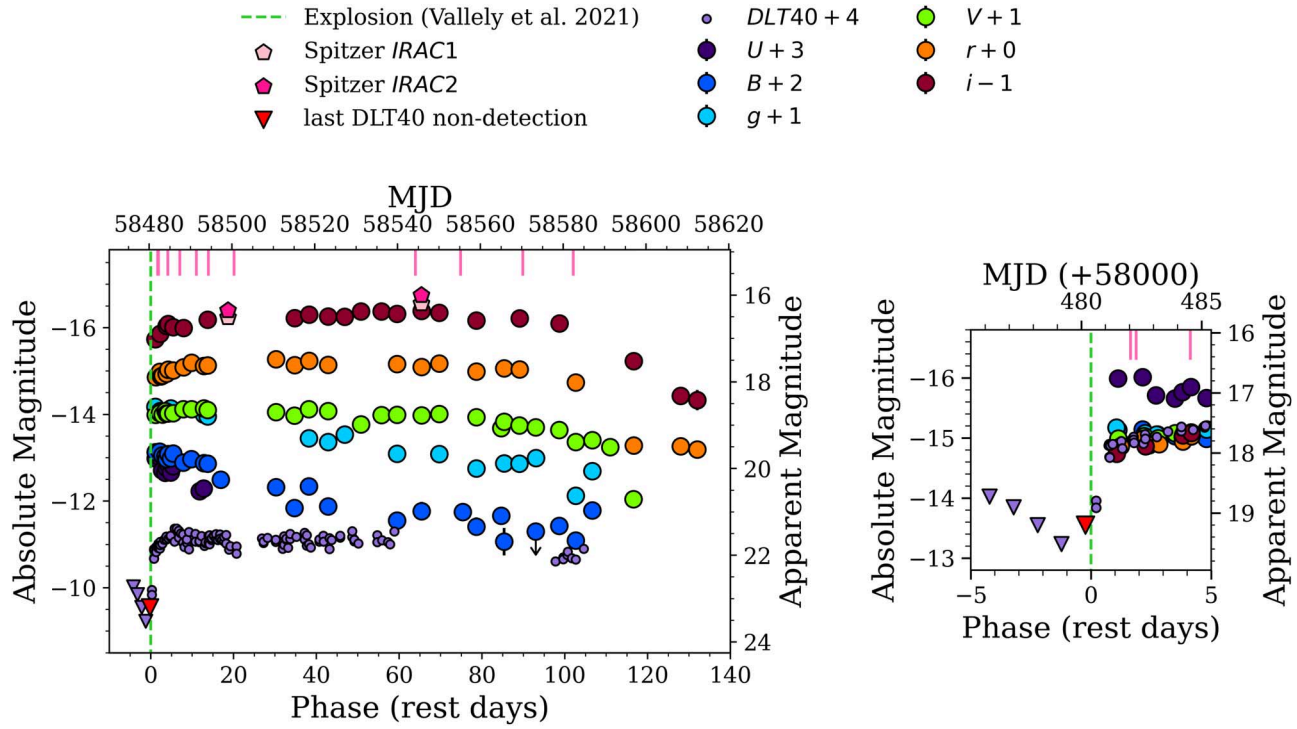

Figure 3. SN 2018lab light curves from DLT40, Las Cumbres Observatory, and Spitzer/IRAC. Left: light curves with offsets. Right: zoom in of the light curve of the first 5 days after explosion without offsets. The spectroscopic epochs are shown as pink lines along the upper *x*-axis. The photometry is available as the data behind the figure.

(The data used to create this figure are available.)

Table 1
Log of Spectroscopic Observations

Date	JD	Epoch (day)	Telescope	Instrument	Exposure (s)
2018-12-30	2458482.5411	1.6	SALT	RSS	1994.0
2018-12-30	2458482.7795	1.9	ESO-NTT	EFOSC2	600.0
2019-01-01	2458485.0255	4.1	FTS 2 m	FLOYDS	3600.0
2019-01-04	2458487.9443	7.0	FTN 2 m	FLOYDS	3600.0
2019-01-08	2458491.9115	11.0	FTN 2 m	FLOYDS	3600.0
2019-01-11	2458494.8412	13.9	Keck I	LRIS+LRISBLUE	600.0
2019-01-17	2458500.9915	20.1	FTS 2 m	FLOYDS	3600.0
2019-03-02	2458544.8102	63.9	FTN 2 m	FLOYDS	3600.0
2019-03-13	2458555.7320	74.8	FTN 2 m	FLOYDS	3600.0
2019-03-28	2458570.7291	89.8	FTN 2 m	FLOYDS	3600.0
2019-04-09	2458582.9357	102.0	FTS 2 m	FLOYDS	3600.0
2019-11-01	2458788.9488	308.0	LBT-SX	MODS1R	600.0

3.2. Distance

We assume a distance modulus of 32.75 ± 0.4 mag, based on the distance of 35.5 Mpc to IC 2163/NGC 2207 (Theureau et al. 2007). This distance is a mean of the *JHK* Tully–Fisher distances and was used in Jencson et al. (2017). This is consistent with the widely used distance to IC 2163/NGC 2207 of 35 ± 2.5 Mpc (Elmegreen et al. 2017; Kaufman et al. 2016) and the measured distance to NGC 2207, using Type Ia SN 1975A, of 39.6 ± 5.5 Mpc (Arnett 1982). A recent paper on SN 2010jp (Corgan et al. 2022), which is in the vicinity of IC 2163/NGC 2207, uses a distance of 24.5 Mpc. However, Corgan et al. (2022) also suggests that the host galaxy of SN 2010jp is a foreground dwarf galaxy, not IC 2163 or NGC 2207, which accounts for the difference in distances.

3.3. Extinction

The equivalent widths of Na I D absorption lines correlate with interstellar dust extinction (Richmond et al. 1994; Munari & Zwitter 1997). To estimate the extinction along the line of sight, the Na I D features in the Keck LRIS spectrum, which has a high signal-to-noise ratio and resolving power of $R = 715$, were analyzed. The equivalent widths of both the $z = 0$ (Milky Way) and the $z = 0.0089$ (host) features were measured by fitting and integrating Gaussian line profiles. The equivalent widths were then converted to $E(B - V)$ using Equation (9) of Poznanski et al. (2012) with an additional normalization factor of 0.86 from Schlafly et al. (2010). This method gives a Milky Way extinction, $E(B - V)_{\rm MW} = 0.058^{+0.012}_{-0.0095}$ mag, which is roughly consistent with the value from Schlafly & Finkbeiner (2011) of

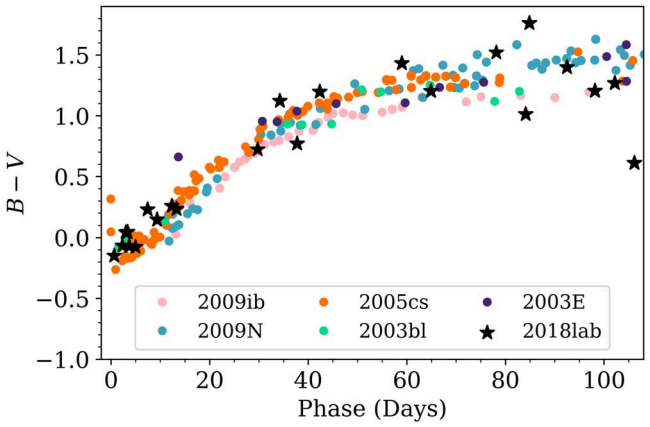

Figure 4. Extinction-corrected $B-V$ color for SN 2018lab compared with other SNe with similar light-curve properties. The adopted $E(B-V)_{\rm tot}=0.22$ mag is consistent with the color evolution of these similar SNe. Data are shown for SN 2009ib (Takáts et al. 2015), SN 2009N (Takáts et al. 2014), SN 2005cs (Tsvetkov et al. 2006; Brown et al. 2007; Pastorello et al. 2009; Faran et al. 2014), SN 2003bl (Galbany et al. 2016), SN 2003E (Galbany et al. 2016), SN 2003bl (Anderson et al. 2014), and SN 2003E (Anderson et al. 2014).

0.0748 ± 0.0006 mag. We adopt the latter value. The equivalent width of the host Na I D doublet was close to 2 Å. The relation between the Na I D equivalent width and dust extinction given in Poznanski et al. (2012) saturates at an equivalent width of ∼0.2 Å, so alternative methods of measuring SN 2018lab's host extinction are required.

The diffuse interstellar band (DIB) absorption feature used in Phillips et al. (2013) can also be used to determine extinction, however the DIB was not visible in any of the SN 2018lab spectra. This was also the case for the K I λ7699 line, which is effective at determining host extinction as well (Munari & Zwitter 1997).

Host extinction is instead determined by comparing the color evolution of SN 2018lab to other SNe IIP with similar peak magnitudes and light-curve shapes (the light-curve properties are described in Section 4), namely SN 2009ib (Takáts et al. 2015), SN 2009N (Takáts et al. 2014), SN 2003bl (Anderson et al. 2014; Galbany et al. 2016), and SN 2003E (Anderson et al. 2014; Galbany et al. 2016). This analysis gives an $E(B-V)_{\rm host}$ of about 0.15 mag (see Figure 4). Using this value, the dereddened spectra of 2018lab matches the continuum slope of other extinction-corrected LLSNe. Given the location of SN 2018lab in a dusty spiral arm of a star-forming galaxy, this level of local host galaxy reddening is not surprising. There is likely significant uncertainty in this value, however the scatter in the $B-V$ color makes it difficult to make a better estimation of the host extinction (Figure 4). We note that SN 2018lab exhibits evidence of CSM interaction, which can make an SN appear slightly more blue and may cause the extinction to be underestimated using this method. The combined Milky Way and host extinction gives an $E(B-V)_{\rm tot}=0.22$ mag, which we adopt as the total extinction to the supernova.

4. Photometric Evolution

In the V band, SN 2018lab peaks at -15.1 ± 0.1 mag, consistent with the observed brightness of the archetype LLSN SN 2005cs (see Figure 5). Compared to SN 2005cs, the bolometric light curve of SN 2018lab remains fairly flat at the start of the plateau phase and has a shorter plateau duration.

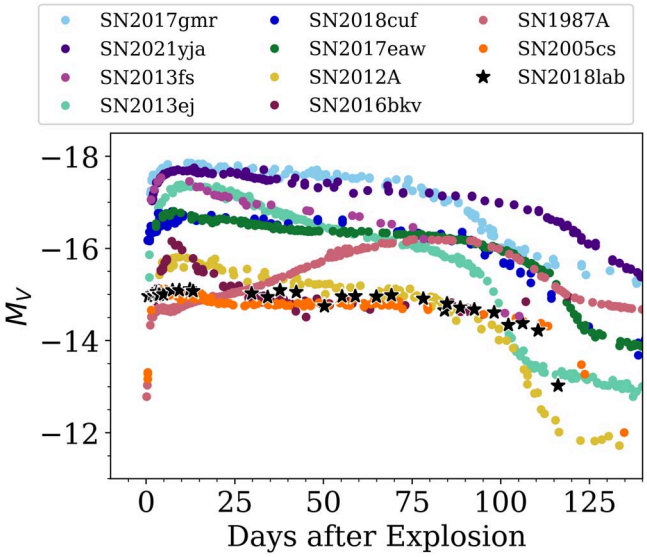

Figure 5. Absolute V-band light curve of SN 2018lab compared with other SNe II: SN 2017gmr (Andrews et al. 2019), SN 2021yja (Hosseinzadeh et al. 2022), SN 2013fs (Rubin et al. 2016; Valenti et al. 2016; Bullivant et al. 2018), SN 2013ej (Huang et al. 2015; Yuan et al. 2016; de Jaeger et al. 2019), SN 2018cuf (Dong et al. 2021), SN 2017eaw (Tsvetkov et al. 2018; Szalai et al. 2019), SN 2012A (Tomasella et al. 2013; de Jaeger et al. 2019), SN 2016bkv (Hosseinzadeh et al. 2018; Nakaoka et al. 2018), SN 1987A (Catchpole et al. 1987, 1988; Menzies et al. 1987; Suntzeff et al. 1988), and SN 2005cs (Tsvetkov et al. 2006; Brown et al. 2007; Pastorello et al. 2009; Faran et al. 2014). SN 2018lab has a peak V-band magnitude of -15.1 mag, which is consistent with the luminosity of SN 2005cs, a notable LLSN.

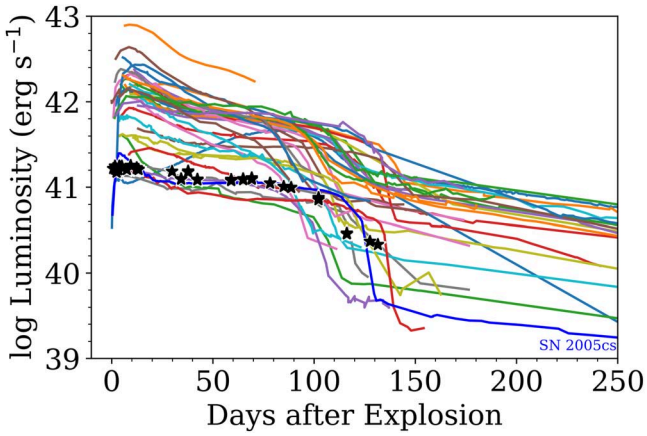

Figure 6. Bolometric light curve of SN 2018lab compared with other SNe II presented in Valenti et al. (2016). SN 2018lab has a peak luminosity of $10^{41.2\pm0.1}$ erg s^{-1}. While SN 2018lab has a flatter and shorter plateau than SN 2005cs (blue), these features are not atypical for an LLSN.

However, given an SN 2018lab peak luminosity of $10^{41.2\pm0.1}$ erg s^{-1}, it fits well into the LLSN subclass, as shown in Figure 6.

The V-band decline rate of SN 2018lab in the 50 days following maximum brightness, denoted s_{50}, was measured according to the protocol outlined in Valenti et al. (2016). SN 2018lab has an extremely flat plateau phase, with an $s_{50}=0.13\pm0.05$ mag/50 days. There are very few light-curve points at the end of the plateau, making it difficult to fit the transition to the nickel tail, and therefore we are unable to estimate a reliable ^{56}Ni mass. The last few points of the r-band light curve have a slope of <0.01 mag day^{-1}, indicating that

Table 2
SN 2018lab's Parameters

Last non-detection	JD 2458480.6624
Discovery	JD 2458481.626
Explosion epoch[a]	JD 2458480.9 ± 0.1
Redshift (z)	0.0089 ± 0.0001
Distance (modulus, μ)	35.5 Mpc (32.75 mag)
$E(B-V)_{\rm tot}$	0.22 mag
$M_{\rm TESS}$ at peak[a]	−15.48 ± 0.29 mag
$t_{\rm rise}$[a]	8.3 ± 0.21 days
s_{50}[b]	0.13 ± 0.05 mag/50 days
$t_{\rm PT}$	113 ± 3 days

Notes.
[a] Taken from Vallely et al. (2021).
[b] As defined by Valenti et al. (2016).

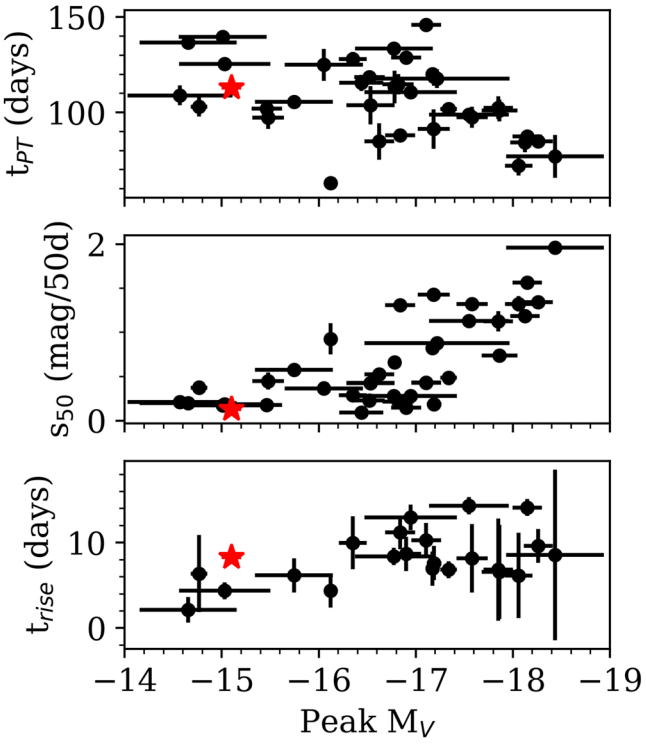

Figure 7. Comparison of the light-curve properties of SN 2018lab to the LLSNe in Valenti et al. (2016). Top: SN 2018lab has a plateau length, $t_{\rm PT}$, in agreement with other SNe II. Middle: in the 50 days following peak magnitude, the slope of SN 2018lab's light curve remains very flat, as is common in LLSNe. Bottom: similar to other LLSNe, SN 2018lab rises to peak light quickly. Error bars on the SN 2018lab measurements are smaller than the marker.

they may lie on the nickel tail. In order to get a rough estimate of the plateau length, we use the average time between the last point on the V-band plateau and the first point on the tail in the r band to determine the plateau length, finding $t_{\rm PT} = 113 \pm 3$ days.

Vallely et al. (2021) models the light curves of 20 CCSNe observed by TESS including SN 2018lab (denoted as DLT18ar in their work) using a curved power law (see their Equation (2)). This method effectively reproduces the shape of SN 2018lab's early light curve, and they find a rise time of $t_{\rm rise} = 8.3 \pm 0.21$ days, which is among the fastest in their sample of 20 SNe. Additionally, SN 2018lab was the lowest-luminosity SN in the sample by almost 2 mag, with a peak luminosity of -15.48 ± 0.29 mag in the TESS band.

The light-curve properties of SN 2018lab (see Table 2) are in line with other LLSNe (see Figure 7). The peak V-band luminosities of LLSNe, including SN 2018lab, are less than a typical CCSN by a factor of 10 (Pastorello et al. 2004). The typical plateau time of SNe II, including LLSNe, is 80–140 days (Valenti et al. 2016), in agreement with SN 2018lab's $t_{\rm PT}$. The peak luminosity and the decline rate of SNe II are related to each other, with LLSNe having much flatter plateaus (i.e., lower s_{50} values) than more-luminous SNe II (Anderson et al. 2014). The s_{50} values for SNe II are $\lesssim$3 mag/50 days. Like other LLSNe, the s_{50} of SN 2018lab lies on the low end of the s_{50} continuum for SNe II. The rise times of SNe II are fast (<20 days) compared to other types of SNe; the rise times of LLSNe are on the faster end of the SN II distribution with $t_{\rm rise} \lesssim 10$ days (Valenti et al. 2016). The values of s_{50}, $t_{\rm PT}$, and $t_{\rm rise}$ for SN 2018lab are similar to other LLSNe in Valenti et al. (2016).

4.1. Shock Cooling Model

The rising light curves of SNe II are in part powered by shock cooling—energy added to the stellar envelope by the CC shock wave. To determine the effect of shock cooling on the rising light curve of SN 2018lab, the light curve is fit using the Light Curve Fitting package (Hosseinzadeh & Gomez 2020), which employs an analytic method for modeling early SNe II light curves powered by shock cooling described in Sapir & Waxman (2017).

Degeneracies between the Sapir & Waxman model parameters makes it difficult to fit them independently in the case of SN 2018lab. Therefore, we use the version of the Sapir & Waxman model used in Hosseinzadeh et al. (2018) which utilizes scaling parameters: the temperature one day after explosion (T_1), the total luminosity ∼1 day after explosion (L_1), the time at which the envelope becomes transparent ($t_{\rm tr}$), and the explosion time (t_0). This version of the model, with a polytropic index of $n = 1.5$ for an RSG progenitor density profile, was fit to the multiband light curve of SN 2018lab up to MJD 58485 (4.6 days after explosion). This was done with a Markov Chain Monte Carlo (MCMC) routine and flat priors for all parameters. The model gives the total luminosity and blackbody temperature as a function of time for each set of parameters. This is then converted to observed fluxes for each photometric point. Figure 8 shows the results of the MCMC routine, including the light-curve fits, posterior distributions, and the 1σ credible intervals centered on the medians.

The best-fit models have difficulty reproducing the fast rise, completely missing the DLT40 and TESS rise points. The best-fit explosion time is MJD 58478.5 ± 0.2, >1 day before the highly constrained explosion time estimated from the TESS data (MJD 58480.4 ± 0.1; Vallely et al. 2021) and before the two DLT40 non-detections. Further, the model fails to fit the rising light curve when the explosion time is fixed to be within the error of the TESS explosion epoch. Due to the failure of the model to fit the steep rise in the light curve accurately, we do not consider these models to be a good fit, but they are included here for completeness.

The failure of the shock cooling model to predict the steep rise accurately may be evidence of ejecta–CSM interaction, which is not accounted for in the Sapir & Waxman model. A steep rise can occur when the CSM is optically thick enough that shock breakout does not occur at the edge of the stellar

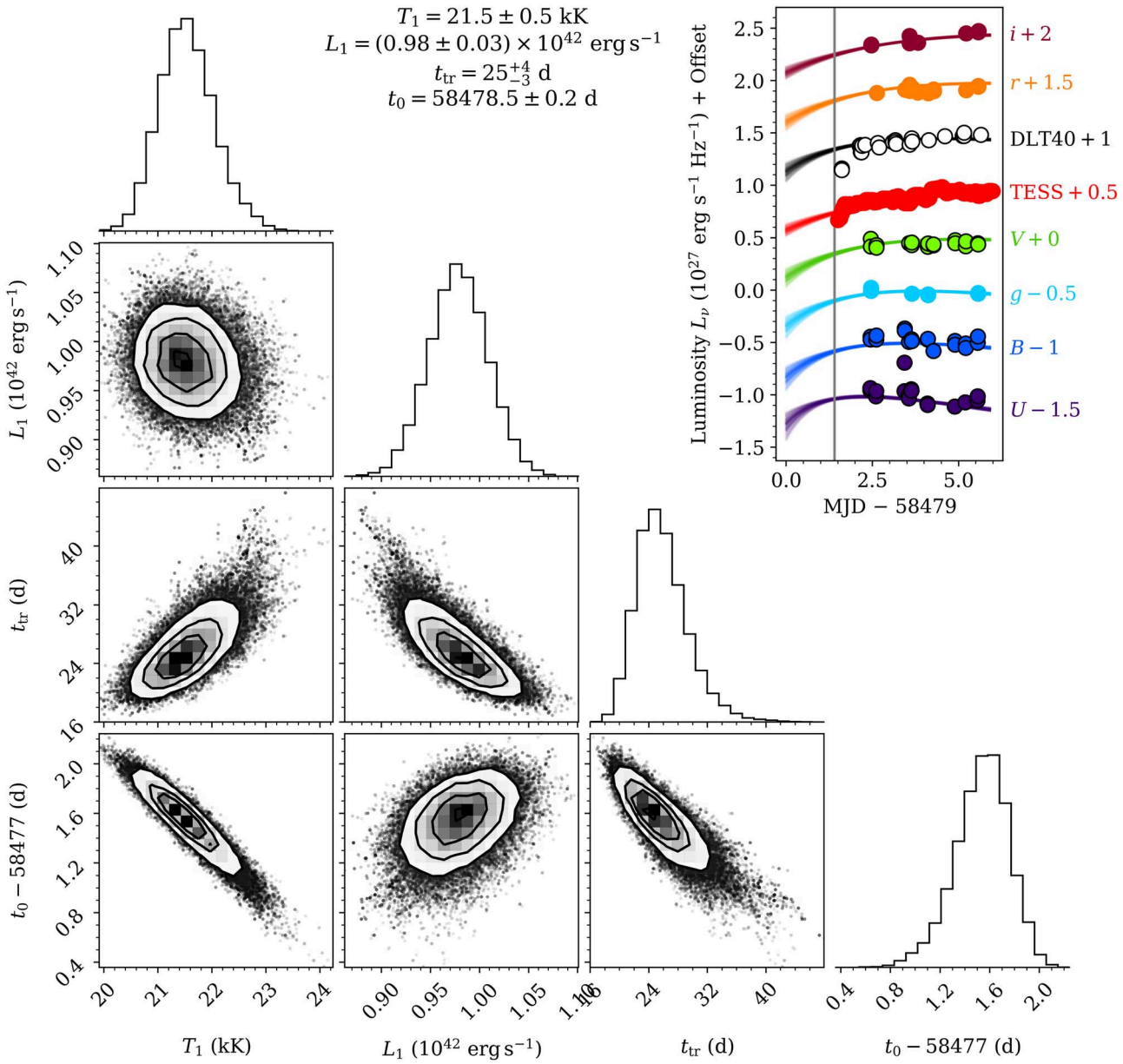

Figure 8. Posterior distributions of and correlations between the temperature one day after explosion (T_1), the total luminosity ∼1 day after explosion (L_1), the time at which the envelope becomes transparent ($t_{\rm tr}$), and the explosion time (t_0). The 1σ credible intervals, centered about the median, are given at the top. The top right panel shows 100 randomly drawn fits from the MCMC code compared to the multiband light curve. The fit predicts an explosion time significantly (>1 day) before the explosion epoch (vertical gray line) constrained by the TESS observations (Vallely et al. 2021) and DLT40 non-detections. The fit fails to describe SN 2018lab's fast-rising light curve (see the TESS and DLT40 light curves). This may indicate the presence of ejecta–CSM interaction, which is not accounted for in this model.

envelope but rather outside of it, within the CSM. The gradual density gradient of the CSM means this shock breakout occurs at a lower density than for a bare RSG, allowing the shocked material to cool and expand faster, resulting in an early excess flux, and therefore a steeper rise than would be expected for an SN without a CSM (Morozova et al. 2017; Tinyanont et al. 2022). This explanation is bolstered by the presence of broad-lined flash features in the early spectra (<2 days post-explosion), to be discussed in Section 5.1.

5. Spectral Evolution

The spectra <105 days post-explosion of SN 2018lab are presented in Figure 9. Based on the 2D spectra, we attribute the narrow lines, particularly near Hα, to host contamination. While there could be narrow lines from the SN, we are unable to identify them given the nearby H II region.

The spectral evolution of SN 2018lab is similar to that of other LLSNe presented in previous papers (e.g., Benetti et al. 2001; Pastorello et al. 2004, 2009; Spiro et al. 2014; Takáts et al. 2014; Lisakov et al. 2017; Valerin et al. 2022). The first four spectra ($\leqslant$7 days) exhibit a blue continuum and the slow emergence of Balmer lines and He I λ5876, as is typical of all SNe II. These early lines have P Cygni profiles with very shallow absorption components. In the 11 days spectrum, the Ca II H&K (λ3934, λ3968) and the Fe II multiplet 42 (λ4924, λ5018, λ5169) lines become visible while He I λ5876 disappears. In the second half of the plateau (>50 days), the O I λ7774, Ca II infrared triplet (λ8498, λ8542, λ8662), [Ca II] (λ7291, λ7324), and Na I D (λ5890, λ5896) lines appear and

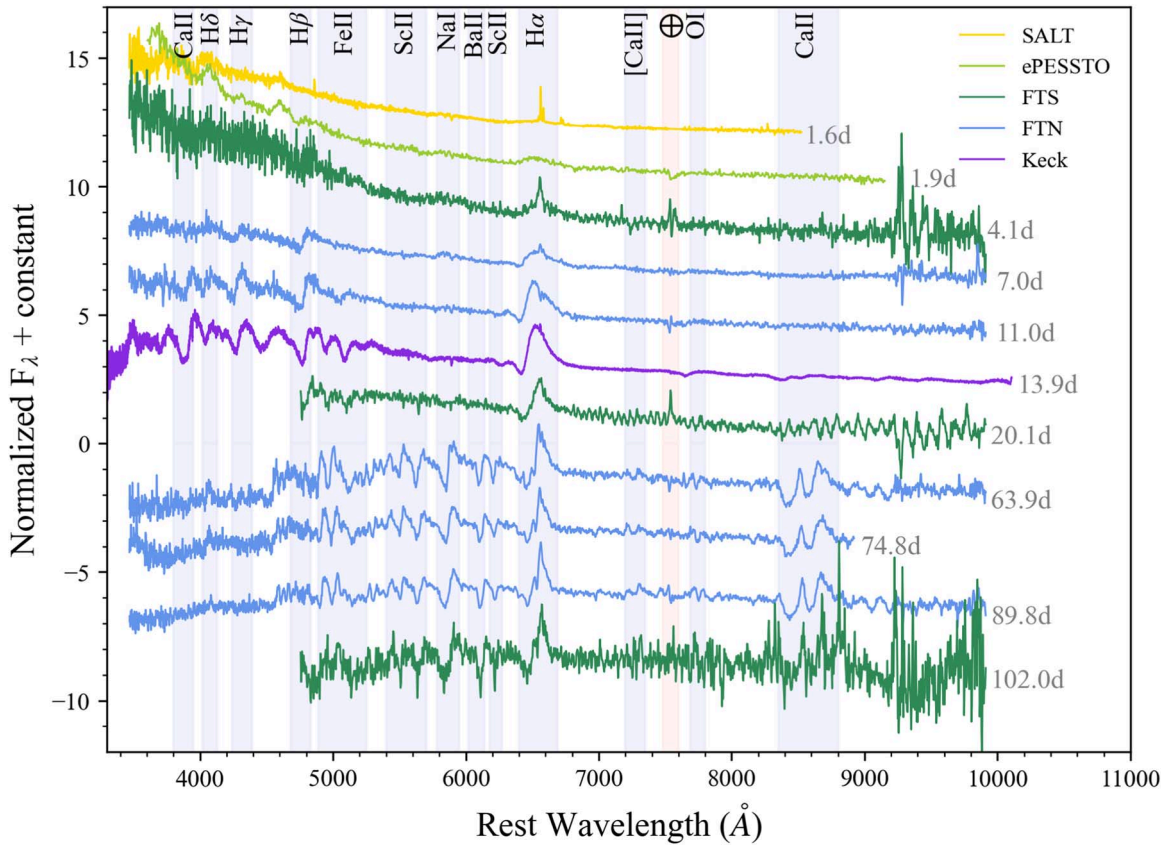

Figure 9. Spectroscopic evolution of SN 2018lab, corrected for $E(B-V)_{\rm tot} = 0.22$ mag. The early spectra ($\leqslant$7 days) of SN 2018lab are dominated by blue continua and H and He I emission lines. At 11 days, Ca II H&K and Fe II lines begin to appear. At later times (>50 days), more metal lines begin to appear: O I, Ca II infrared triplet, [Ca II], and Na I D. Strong Sc II and Ba II lines also emerge during this epoch. All of these spectral features and the timings of their emergence are typical of LLSNe (Pastorello et al. 2004; Spiro et al. 2014; Gutiérrez et al. 2017). The spectra are available as the data behind the figure. The late-time spectrum shown in Figures 16 and 17 is also included here.

(The data used to create this figure are available.)

strengthen. Further, this epoch also exhibits the characteristic strong Sc II and Ba II lines seen in LLSNe (Pastorello et al. 2004; Spiro et al. 2014; Gutiérrez et al. 2017).

There are a few notable features in the spectral evolution of SN 2018lab worth further discussion: the broad-lined flash feature in the early spectra, the appearance of an additional absorption component on the blue side of Hα, and the evolution of the Hα profile in the second half of the plateau phase. These features are discussed in Sections 5.1, 5.2, and 5.3, respectively.

5.1. Flash Spectroscopy

SN 2018lab does not exhibit narrow high-ionization lines in the early (<2 days) spectra. Instead, the early spectra of SN 2018lab show a broad feature from 4500 to 4750 Å (see Figure 10). This feature peaks near the N V λ4604 line. The feature is most clear in the spectrum 1.9 days post-explosion though it is also present in the first spectrum of SN 2018lab (1.6 days post-explosion). The SN 2018lab spectrum from 4.1 days post-explosion has a low signal-to-noise ratio in the relevant wavelength range and we are unable to discern if the earlier broad feature remains. Only one LLSN has exhibited narrow high-ionization lines, SN 2016bkv (Hosseinzadeh et al. 2018). In the spectra of SN 2016bkv, broad-lined flash features first appear in the spectra taken four days post-explosion in a shape similar to those seen in SN 2018lab, and the narrow lines become prominent a day later.

An early broad feature near 4600 Å, sometimes referred to as a "ledge" feature (Andrews et al. 2019; Soumagnac et al. 2020; Hosseinzadeh et al. 2022), has been observed in the early spectra of other SNe II (see Figures 10 and 11). Very few LLSNe have spectra <5 days following explosion. However of those that do—SN 2002gd (Spiro et al. 2014), SN 2005cs (Pastorello et al. 2006), SN 2010id (Gal-Yam et al. 2011), SN 2016bkv (Hosseinzadeh et al. 2018), and SN 2020cxd (Valerin et al. 2022)—the majority (SN 2005cs, SN 2010id, and SN 2016bkv) appear to have a feature similar to what we observe for SN 2018lab (see Figure 10). The cause of this feature has been explained in three ways. In the spectra of SN 2005cs, Pastorello et al. (2006; their Figure 5) interprets this feature as high-velocity (HV) Hβ. There is no indication of an HV feature blueward of Hα in SN 2018lab at early times, so we disfavor this explanation. An alternative explanation is provided for SN 2010id by Gal-Yam et al. (2011; their Figure 2), who suggest that this feature is broad, blueshifted He II λ4686. This analysis has been used to explain similar features in more typical SNe II as well, as seen in Quimby et al. (2007; their Figure 10), Bullivant et al. (2018; their Figure 20), and Andrews et al. (2019; their Figure 18). The other interpretation is that the feature is the blend of several ionized features from the CSM (Dessart et al. 2017). This is the explanation used by

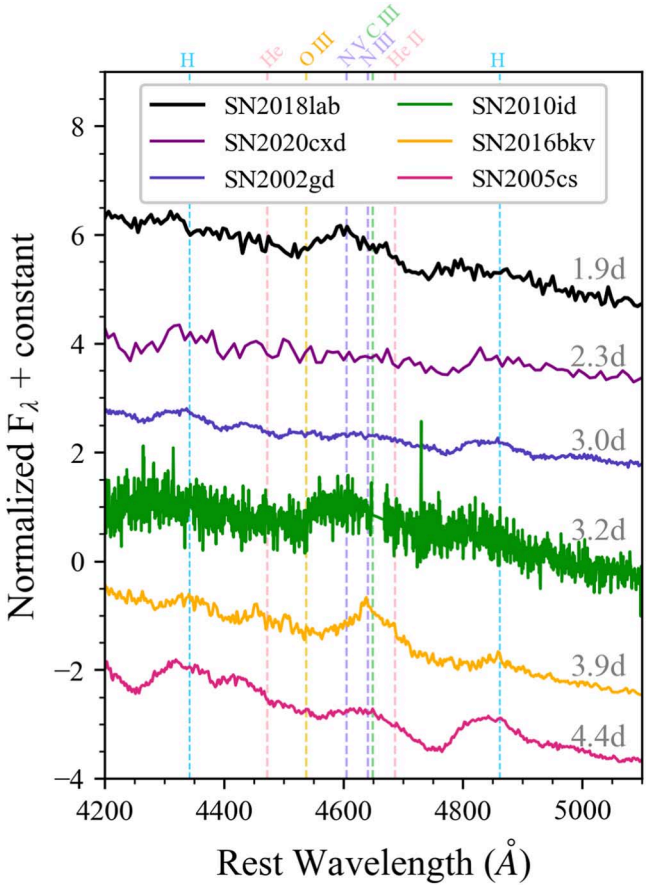

Figure 10. Comparison of the broad early feature seen in SN 2018lab with other LLSNe which have spectra <5 days post-explosion: SN 2002gd (Spiro et al. 2014), SN 2005cs (Pastorello et al. 2006, 2009), SN 2010id (Gal-Yam et al. 2011), SN 2016bkv (Hosseinzadeh et al. 2018), and SN 2020cxd (Valerin et al. 2022). Of these LLSNe, four (SN 2005cs, SN 2010id, SN 2016bkv, and SN 2018lab) out of the six have a strong broad early spectral feature near 4600 Å, though the shape, strength, and interpretation of this feature varies. It is likely that more LLSNe also exhibit similar features however a larger sample of early-time (<5 days) spectra is needed to constrain the frequency at which this feature occurs. All spectra are extinction-corrected.

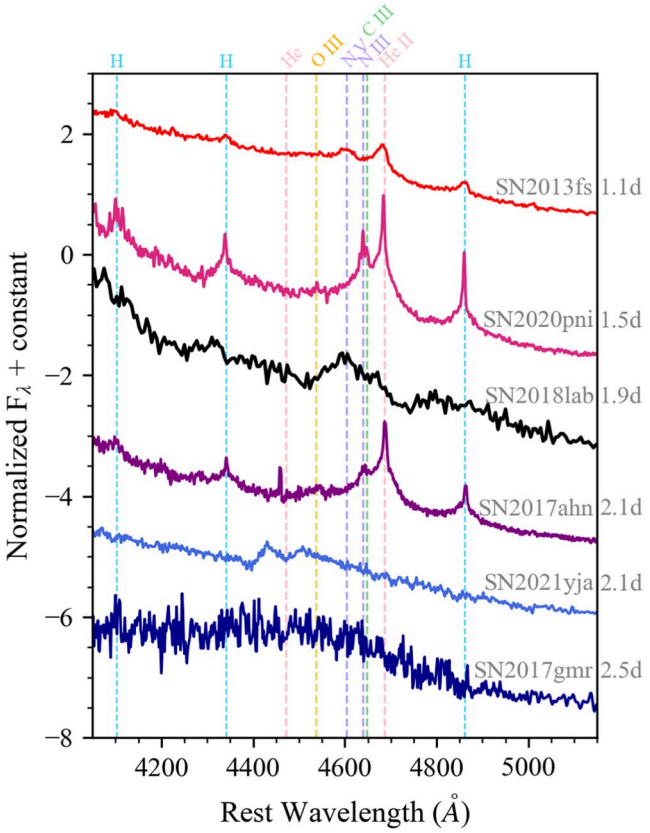

Figure 11. The 1.9 days spectrum of SN 2018lab compared to the early-time spectra of SN 2013fs (Bullivant et al. 2018), SN 2020pni (Terreran et al. 2022), SN 2017ahn (Tartaglia et al. 2021), SN 2021yja (Hosseinzadeh et al. 2022), and SN 2017gmr (Andrews et al. 2019). SN 2020pni and SN 2017ahn exhibit clear narrow-lined flash features; whereas SN 2013fs, SN 2021yja, and SN 2017gmr all have broader early spectral features. The morphology of the feature in the spectra of SN 2018lab further highlights the significant diversity of the flash spectroscopy observed in SNe II. All spectra have been corrected for extinction.

Hosseinzadeh et al. (2018; their Figure 2) to explain the shape of the feature in the spectra of SN 2016bkv, and has also explained similar features in more typical SNe II, as seen in Soumagnac et al. (2020; their Figure 7), Bruch et al. (2021; their Figure 5), and Hosseinzadeh et al. (2022; their Figure 11). SN 2018lab's early broad feature is somewhat double peaked indicating that there may be more than one line contributing to the feature. Therefore we posit that this feature is likely the blend of several ionized features from the CSM: N V, N III, C III, O III, and He II, rather than just blueshifted He II (see Figure 10).

The morphology of SN 2018lab's ledge feature adds to the significant diversity observed in the early spectra of SNe II (see Figure 11). Symmetric narrow-lined flash features, like those seen in SN 2017ahn (Tartaglia et al. 2021) and SN 2020pni (Terreran et al. 2022) are produced via noncoherent scattering of thermal electrons. In contrast, bulk motions produce broad lines which can blend together and produce a broad asymmetric feature (Dessart et al. 2009). When observed, both narrow- and broad-lined flash features can be used as a probe of the properties of the progenitor and the extent of the CSM.

As shown in Figure 12, the broad early spectral feature in the 1.9 days spectrum of SN 2018lab closely resembles the Dessart et al. (2017) `r1w1h` and `r1w5h` models, both of which have RSG progenitors with extended atmospheres and CSMs. The correspondence with the `r1w5h` model is especially striking. The Dessart et al. (2017) r1w1 and r2w1 models also display ledge features, however these features are blueshifted with respect to the observed SN 2018lab feature and are therefore not included in Figure 12.

Both the `r1w1h` and `r1w5h` models display narrow-lined flash features which appear immediately following explosion (<4 hr) and quickly evolve into a broad spectral feature. These models focus on the first ∼15 days after explosion and only extend out to 1.5×10^{15} cm. Both `r1w1h` and `r1w5h` assume a progenitor star with radius $R_* = 501\,R_\odot$ and wind mass-loss rates of 10^{-6} and $5 \times 10^{-3}\,M_\odot\,\mathrm{yr}^{-1}$, respectively. Both have extended atmospheres, with scale heights of $H_\rho = 0.3\,R_*$ for `r1w1h` and $H_\rho = 0.1\,R_*$ for `r1w5h`. A moderate amount of energy deposited into an RSG envelope in late-stage nuclear burning can cause envelope expansion and mass ejection (Smith & Arnett 2014; Morozova et al. 2020). Just like a dense CSM, an extended envelope can produce excess luminosity in SN light curves (Morozova et al. 2020). The shape of SN 2018lab's early broad feature is qualitatively reproduced by the `r1w1h` and `r1w5h` models. Note that these models

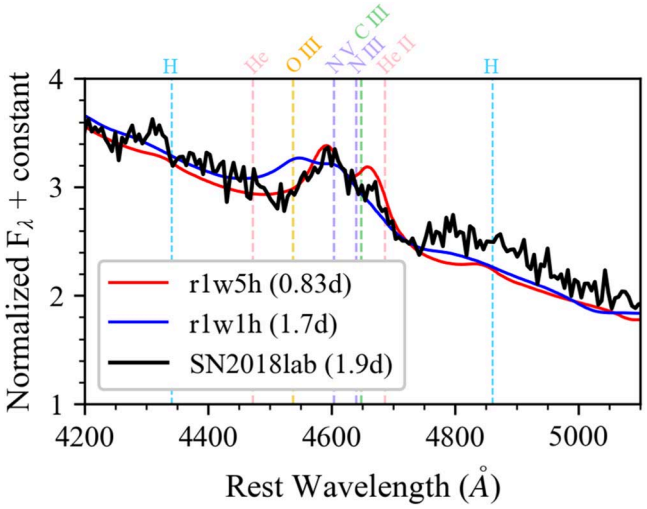

Figure 12. The early broad feature (4500–4750 Å) in the 1.9 days spectrum of SN 2018lab is compared to the Dessart et al. (2017) models that most closely resemble the spectra, `r1w1h` and `r1w5h`, which are both RSGs with extended atmospheres. The closest analog to the SN 2018lab data is the the `r1w5h` model at 0.83 days. `r1w1h` and `r1w5h` are scaled by 70% to fit the flux of the feature better and have been convolved to the resolution of the observed spectrum (14 Å, Smartt et al. 2015).

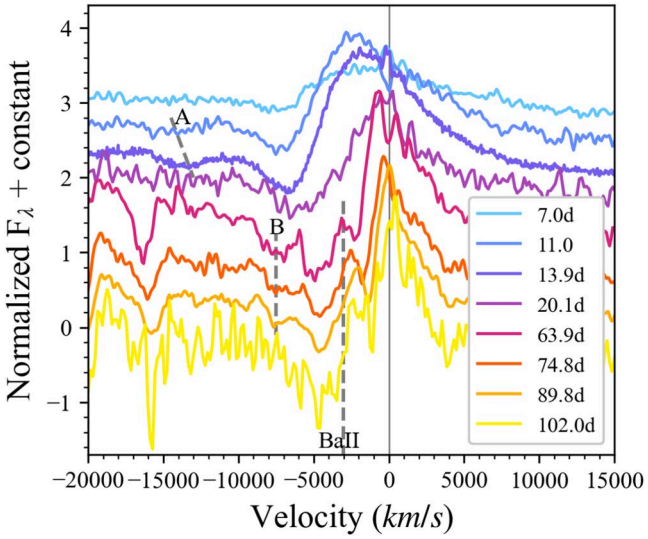

Figure 13. Evolution of Hα starting at seven days post-explosion. The spectra exhibit both A- (10–15 days) and B-type (50–90 days) Cachito features (dotted lines). These features are likely due to Si II λ6355 and HV H, respectively. At >50 days the existence of a complex Hα profile becomes evident. This is attributed to the presence of Ba II λ6497 (rest frame denoted with the gray dashed lines).

assume a much more energetic explosion (1.35×10^{51} erg) and a much more massive progenitor (ejecta mass of 12.52 $M_\odot$) than is typical for LLSNe, therefore the CSM around SN 2018lab is unlikely to have identical properties to the modeled CSM. However, the similarity of the observed ledge feature to that of the r1w1h and r1w5h models could indicate that the feature may be caused by the extended envelope of an RSG progenitor and CSM interaction.

The ledge feature seen in the SN 2018lab data is most similar to `r1w5h` at 0.83 days. The similarity to the `r1w5h` model suggests the presence of a higher-density CSM than assumed by the `r1w1h` model, but still low enough to prevent the appearance of narrow-lined flash features more than a few hours after explosion. The early broad-lined flash features in the spectra of SN 2016bkv are also similar to the shape of the `r1w5h` model at 0.83 days. However, this spectral feature in SN 2016bkv appears four days post-explosion, substantially after the model epoch, which may suggest a much larger and denser CSM than described by the model (Hiramatsu et al. 2021b). In SN 2018lab, the features are present much earlier, indicating a progenitor with an extended envelope similar to that described by the `r1w5h` model with a CSM that is less dense than for SN 2016bkv.

5.2. Cachito Features

"Cachito" features (Gutiérrez et al. 2017) are small absorption features blueward of Hα which are common in the optical spectra of SNe II (e.g., Bostroem et al. 2019, 2020; Dong et al. 2021). There are two main types of Cachito features, the kind which arise earlier (<40 days) in the spectral evolution and those which emerge later (>40 days). Both types of Cachito features appear on the blue side of Hα in the spectra of SN 2018lab, and are distinct (see Figure 13). Gutiérrez et al. (2017) found that, among SNe that exhibit Cachito features at <40 days post-explosion, in 60% of cases the feature results from Si II λ6355 and the remaining cases are likely due to HV Hα. In SNe with Cachito features that emerge at >40 days, this feature may occur when X-rays from the SN shock ionize and excite the outer unshocked ejecta and HV H absorption features form (see Chugai et al. 2007).

The early Cachito feature, denoted as A in Figure 13, appears in the 11 and 13.9 days spectra at 13,000–14,000 km s^{-1} with respect to rest Hα. If the "A" Cachito feature is due to Si II λ6355 it should have a velocity similar to other metal lines in the spectrum (Gutiérrez et al. 2017). The measured velocity of the shallow "A" Cachito feature in the 13.9 days spectrum of SN 2018lab is 4500 km s^{-1} in the Si II λ6355 rest frame. This velocity is similar to the velocity of Fe II λ5018 and λ5169 in the same epoch. We determine that the Cachito feature in the 11 and 13.9 days spectra of SN 2018lab is likely the result of Si II λ6355.

The late Cachito feature, denoted as B in Figure 13, appears in the spectra from 50–90 days post-explosion. While Ba II λ6497 is visible in this region during the relevant epochs, a velocity analysis indicates that the "B" Cachito feature in SN 2018lab is not associated with Si II λ6355 or Ba II λ6497. If the "B" Cachito is related to HV H, its velocity should be similar to that of Hα at earlier phases and a companion feature may be visible blueward of Hβ, though this is rare in the LLSNe subclass (Gutiérrez et al. 2017). The velocity relative to Hα of the "B" Cachito feature, ~7500 km s^{-1}, is consistent with the velocity of Hα in the 7 and 11 days spectra. This indicates that the Cachito feature in the 50–90 days spectra of SN 2018lab is likely the result of HV H. The numerous metal lines and low signal-to-noise ratios at the blue end of the spectra make it difficult to discern if there is a counterpart HV feature near Hβ. This HV H feature is likely to be related to SN ejecta and RSG wind interaction (Gutiérrez et al. 2017) and may be further evidence for a CSM surrounding the progenitor.

5.3. Complex Hα Profile

The Hα in SN 2018lab exhibits a clear P Cygni profile beginning at the start of the plateau phase. In the spectra taken 7–20 days post-explosion, the Hα velocity is 6000–8000 km s^{-1}.

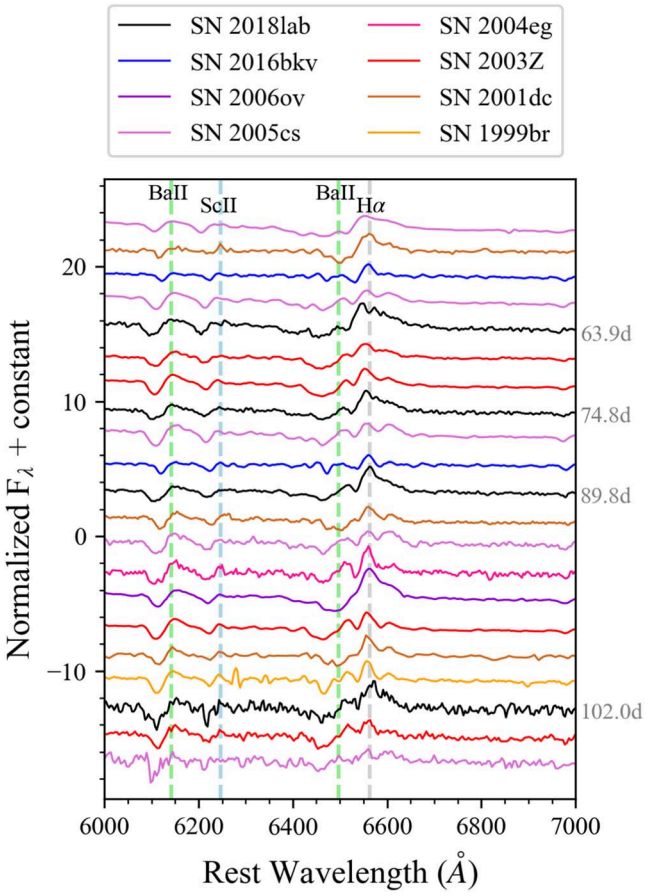

Figure 14. Spectra from the later half of the plateau phase of other notable LLSNe compared to SN 2018lab. Many LLSNe have strong Ba II and Sc II lines during this phase of evolution, which yield a complex Hα profile. Data are taken from Pastorello et al. (2004; SN 1999br and SN 2001dc), Pastorello et al. (2009; SN 2005cs), Spiro et al. (2014; SN 2003Z, SN 2004eg, and SN 2006ov), and Hosseinzadeh et al. (2018; SN 2016bkv). All spectra are corrected for extinction.

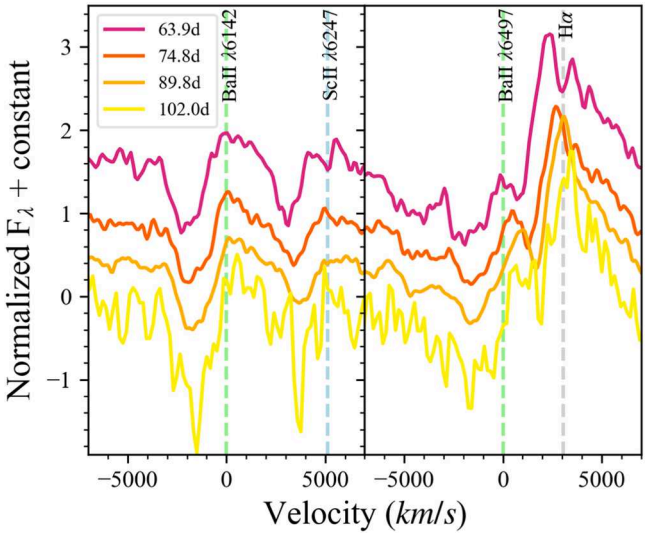

Figure 15. Evolutions of the Ba II λ6142 and λ6497 during the second half of the plateau phase (~50–100 days). Ba II λ6142 has v(Ba II) $\approx$ 2000 km s^{-1}. Ba II λ6497 is likely to be evolving similarly to Ba II λ6142, therefore it is very difficult to determine the velocity of Hα during these epochs. The relevant spectral lines (dotted) are at rest.

This is similar to the Hα velocities observed for SN 2005cs at the same epochs (Pastorello et al. 2009). CSM interaction will decelerate SN ejecta, with high-density CSMs resulting in ejecta speeds ~1000 km s^{-1} slower than low-density CSMs in models of typical SNe II (Dessart et al. 2017). However, lower expansion speeds are characteristic of LLSNe and we are unable to set limits on the density of the CSM from this measurement alone.

The Hα profile of SN 2018lab becomes complex starting in the 63.9 days spectrum, in the second half of the plateau phase (see Figure 13). This complex Hα profile is not uncommon in LLSNe (see Figure 14) and has previously been described as the result of the combination of Hα and Ba II λ6497 (Benetti et al. 2001; Pastorello et al. 2009; Takáts et al. 2014; Lisakov et al. 2017; Valerin et al. 2022). The strength of Ba II lines in LLSNe is a temperature effect, rather than reflecting a relative overabundance. The low temperatures of LLSNe ejecta result in small Ba III/Ba II ratios and therefore strong Ba II lines (Turatto et al. 1998). The presence of exceptionally strong Ba II lines, particularly Ba II λ6142, is a hallmark of the ~80–100 days spectra of LLSNe (Pastorello et al. 2004; Spiro et al. 2014; Gutiérrez et al. 2017; Lisakov et al. 2018) and is also present in the spectra of SN 2018lab (see Figure 9).

The velocity evolutions of Ba II λ6142 and λ6497 are shown in Figure 15. The v(Ba II) of Ba II λ6142, the strongest line in the Ba II multiplet, which includes Ba II λ6497, is ~2000–1500 km s^{-1} for the 64–102 days spectra of SN 2018lab. As expected, there is a clear absorption feature centered at ~2000 km s^{-1} in the rest frame of Ba II λ6497 as well. However, the profile of this region makes it difficult to determine the velocity of both Ba II λ6497 and Hα in the epochs where Ba II λ6497 is present.

Higher signal-to-noise ratio spectra of LLSNe within the crucial second half of the plateau phase are required in order to understand the structure of the region surrounding Hα better. Both SYNOW- (Pastorello et al. 2004; Takáts et al. 2014) and CMFGEN-based (Lisakov et al. 2017, 2018) models of LLSNe spectra fail to replicate the Hα profile adequately. Barium (Ba) is an *s*-process element and is not included in current models. Detailed modeling, which includes Ba II, of the Hα region in LLSNe is needed to facilitate a better understanding of the role of metals on the spectral evolution of LLSNe.

5.4. Nebular Spectra

Once SN ejecta are predominately transparent to optical light, several clues to the progenitor emerge in the nebular spectra. We obtained a nebular spectrum of SN 2018lab at 308 days post-explosion. In Figure 16, the nebular spectrum of SN 2018lab is compared to similar spectral epochs of SN 2005cs (Pastorello et al. 2009), which has a confirmed low-mass RSG progenitor, and SN 2016bkv (Hosseinzadeh et al. 2018), which has been suggested as a possible ECSN. The SN 2018lab spectrum presented in this figure has been smoothed using a 10 pixel wide box kernel to reduce the appearance of noise. While its nebular spectrum has many of the same features exhibited by both SN 2016bkv and SN 2005cs, SN 2018lab's strong [C I] λ8727 feature is only present in the nebular spectrum of SN 2005cs. The importance of this is explained below.

In Figure 17, the nebular spectrum of SN 2018lab is compared to the 300 days nebular spectra models for a 9 $M_\odot$ RSG progenitor presented in Jerkstrand et al. (2018). Since we are unable to determine the nickel mass of SN 2018lab

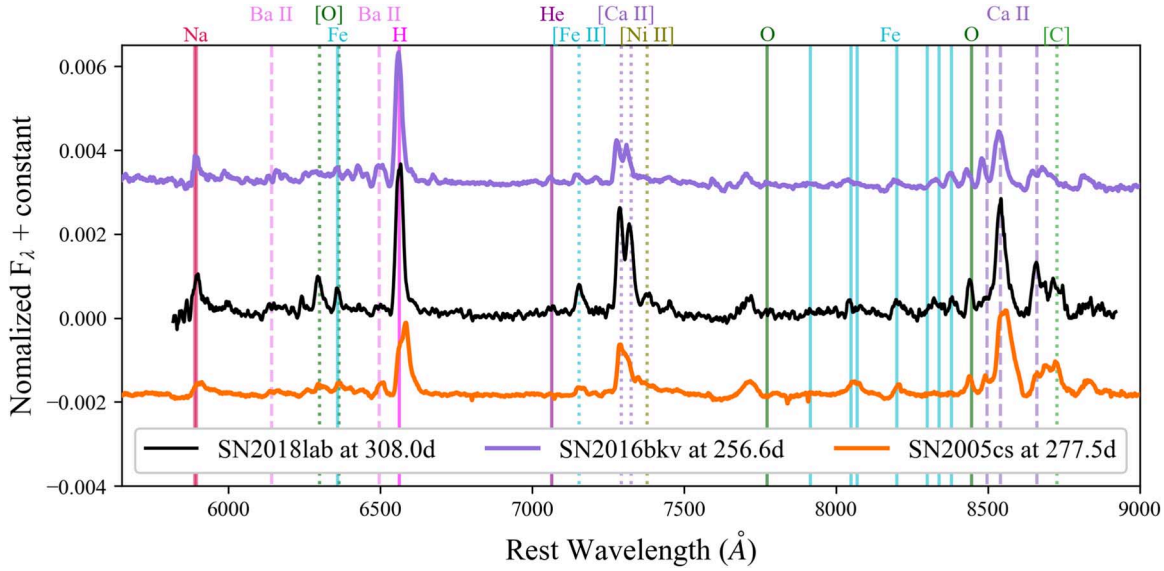

Figure 16. Late-time spectrum of SN 2018lab taken 308 days post-explosion compared to the late-time spectra of SN 2005cs (Pastorello et al. 2009) and SN 2016bkv (Hosseinzadeh et al. 2018). The spectrum of SN 2018lab is smoothed using a 10 pixel wide box kernel. All spectra are normalized to the total flux over the wavelength range of the observed SN 2018lab spectrum. While there are many similarities among all three spectra, [C I] λ8727 is only present in the nebular spectra of SN 2005cs and SN 2018lab.

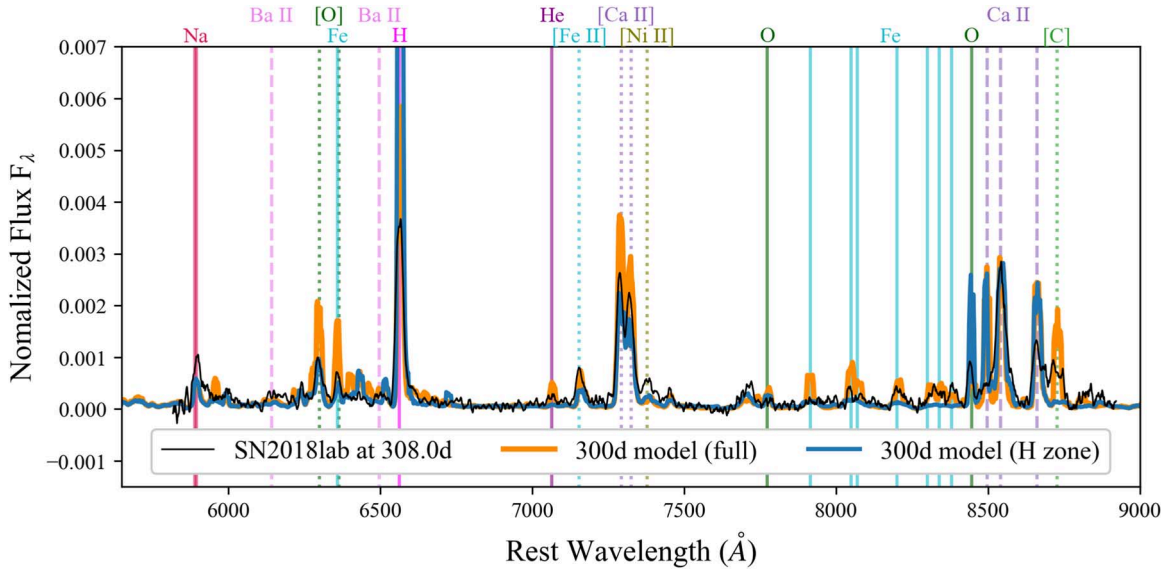

Figure 17. Late-time spectrum of SN 2018lab taken 308 days post-explosion compared to the 9 $M_\odot$ Jerkstrand et al. (2018) models. Both the models and the spectrum are normalized to the total flux over the wavelength range of the observed spectrum to highlight the line ratio differences. The full model, orange, is the expected spectrum for an iron CCSN. The hydrogen-zone model, in blue, of Jerkstrand et al. (2018) should be similar to the nebular spectrum expected of an ECSN. The late-time spectrum of SN 2018lab is similar to that of the iron CC model. In particular, [C I] λ8727 is present in the spectrum of SN 2018lab and is not included in the ECSNe model.

and therefore cannot correct for the nickel luminosity at this phase, these models and the spectrum are all normalized to the total flux over the wavelength range of the observed spectrum. The "pure hydrogen-zone" model presented in Jerkstrand et al. (2018) describes the signatures of a progenitor made up of only material from the hydrogen envelope (see their Figure 2). While the H-zone model is not an EC model, they expect an ECSN to resemble this model. The full Fe CC model is distinctive from the H-zone model, and particularly notable is the lack of He I λ7065, Fe I λ7900–8500, and [C I] λ8727 in the H-zone model.

SN 2018lab clearly exhibits [C I] λ8727 and several Fe I λ7900–8500 lines. There is also some evidence of He I λ7065. The appearance of these lines, though weaker than indicated by the model, strongly suggests the existence of He and O zones in the progenitor star at the time of collapse. This stellar composition indicates that SN 2018lab is likely to be the result of iron CC in an RSG. Pre-explosion HST images of IC 2163/NGC 2207 are unable to offer robust confirmation of this progenitor hypothesis. Given the distance to the host galaxy, the environment surrounding the SN, and the likelihood of a low-mass progenitor star, further HST images of the site of

SN 2018lab are required to shed light on the progenitor of SN 2018lab and the progenitors of LLSNe in general.

6. Summary and Conclusions

We present comprehensive photometric and spectroscopic observations of SN 2018lab. The early light curve of SN 2018lab is one of the best-sampled SNe II to date due to the 30 minute cadence TESS light curve. The TESS light curve combined with extensive photometric and spectroscopic follow-up places tight constraints on the early evolution and explosion epoch of SN 2018lab (see also the recent extensive follow-up campaign of the TESS-observed SN 2019esa; Andrews et al. 2022).

SN 2018lab is among the rare class of LLSNe with observational evidence of short-lived CSM interaction. First, the rising light curve cannot be fit with an analytic model of shock cooling (Sapir & Waxman 2017), indicating that the fast rise is likely the result of excess luminosity due to ejecta–CSM interaction, which is not accounted for in the model. Second, the flash spectroscopy in the first couple days following explosion reveals the presence of a CSM around the progenitor star. In particular, the broad, ledge-shaped spectral feature at ∼4500–4750 Å in the +1.9 days spectrum of SN 2018lab is analogous to models of ejecta interaction of an RSG with an extended envelope and encompassed by a close-in CSM (Dessart et al. 2017). While we do not explicitly rule out a super-AGB or high-mass ($>20\,M_{\odot}$) RSG progenitor, the light-curve shape and spectral evolution of SN 2018lab are similar to typical LLSNe, including SN 2005cs, which has an identified low-mass ($10 \pm 3\ M_{\odot}$) RSG progenitor (Li et al. 2006). Further, the nebular spectrum of SN 2018lab displays many of the features expected to appear in the late-time spectra of iron CCSNe, adding to the likelihood of an RSG progenitor. Given the distance to the host and the nearby H II region, the pre-explosion HST images of SN 2018lab alone do not set strong enough limits to determine the progenitor of SN 2018lab. Additional post-explosion HST images taken after the SN light has sufficiently faded are required to set robust constraints on the progenitor of SN 2018lab necessary to test the progenitor pathway suggested in this work.

Currently, there is no indication that the progenitor of SN 2018lab is not an RSG, suggesting that late-stage mass loss may be common in LLSNe progenitors regardless if they are RSGs or super-AGBs. Evidence of CSM interaction alone is not enough to determine whether or not an LLSN is the result of EC or CC. Some work has been done to determine the characteristics which distinguish EC from CC processes, including line ratios in nebular spectra and progenitor identification (Hiramatsu et al. 2021b), but this is still in its early phase and uncertain. In order to understand truly the progenitor pathways of LLSNe, more spectra and photometry of these objects are urgently needed, not only following explosion but also during the nebular phase.

SN 2018lab is one of the few LLSNe with observed flash features. The increase in SNe II spectra taken in the hours and days following the explosion has uncovered the diverse morphology in broad early spectral features. Further early observations of SNe II, including the least luminous tails of the SN II distribution, will shed light on the extent and mechanics of late-stage mass loss in RSGs.

We thank Luc Dessart for providing his model spectra. Time domain research by the University of Arizona team and D.J.S. is supported by NASA grant 80NSSC22K0167, NSF grants AST-1821987, 1813466, 1908972, & 2108032, and by the Heising-Simons Foundation under grant #2020-1864. J.E.A. is supported by the international Gemini Observatory, a program of NSF's NOIRLab, which is managed by the Association of Universities for Research in Astronomy (AURA) under a cooperative agreement with the National Science Foundation, on behalf of the Gemini partnership of Argentina, Brazil, Canada, Chile, the Republic of Korea, and the United States of America. Research by Y.D., N.M., and S.V. is supported by NSF grants AST-1813176 and AST-2008108. K.A.B. acknowledges support from the DIRAC Institute in the Department of Astronomy at the University of Washington. The DIRAC Institute is supported through generous gifts from the Charles and Lisa Simonyi Fund for Arts and Sciences, and the Washington Research Foundation. The SALT data reported here were taken as part of Rutgers University program 2018-1-MLT-006 (PI: S. W. Jha). This research has made use of the NASA/IPAC Extragalactic Database (NED), which is funded by the National Aeronautics and Space Administration and operated by the California Institute of Technology. This research has also made use of the Spanish Virtual Observatory https://svo.cab.inta-csic.es) project funded by MCIN/AEI/10.13039/501100011033/ through grant PID2020112949GBI00 and the Weizmann Interactive Supernova Data Repository (WISeREP; https://wiserep.weizmann.ac.il; Yaron & Gal-Yam 2012). This paper made use of the modsCCDRed data reduction code developed in part with funds provided by NSF Grants AST-9987045 and AST-1108693. Based in part on data acquired at the Siding Spring Observatory 2.3 m, we acknowledge the traditional owners of the land on which the SSO stands, the Gamilaraay people, and pay our respects to elders past and present.

Facilities: ADS, CTIO:PROMPT, LBT (MODS), Las Cumbres Observatory (Sinistro, FLOYDS), Keck I (LRIS), Meckering:PROMPT, NED, NTT (EFOSC2), SALT (RSS), Spitzer (IRAC), WISeREP.

Software: astropy (Astropy Collaboration et al. 2013, 2018), corner (Foreman-Mackey 2016), emcee (Foreman-Mackey et al. 2013), FLOYDS pipeline (Valenti et al. 2014), `HOTPANTS` (Becker 2015), `lcogtsnpipe` (Valenti et al. 2016), Light Curve Fitting (Hosseinzadeh & Gomez 2020), MatPLOTLIB (Hunter 2007), NumPy (Harris et al. 2020), PySALT (Crawford et al. 2010), Scipy (Virtanen et al. 2020).

ORCID iDs

Jeniveve Pearson https://orcid.org/0000-0002-0744-0047
Griffin Hosseinzadeh https://orcid.org/0000-0002-0832-2974
David J. Sand https://orcid.org/0000-0003-4102-380X
Jennifer E. Andrews https://orcid.org/0000-0003-0123-0062
Jacob E. Jencson https://orcid.org/0000-0001-5754-4007
Yize Dong (董一泽) https://orcid.org/0000-0002-7937-6371
K. Azalee Bostroem https://orcid.org/0000-0002-4924-444X
S. Valenti https://orcid.org/0000-0001-8818-0795
Daryl Janzen https://orcid.org/0000-0003-0549-3281
Nicolás Meza Retamal https://orcid.org/0000-0002-7015-3446

M. J. Lundquist https://orcid.org/0000-0001-9589-3793
Samuel Wyatt https://orcid.org/0000-0003-2732-4956
R. C. Amaro https://orcid.org/0000-0002-1546-9763
Jamison Burke https://orcid.org/0000-0003-0035-6659
D. Andrew Howell https://orcid.org/0000-0003-4253-656X
Curtis McCully https://orcid.org/0000-0001-5807-7893
Daichi Hiramatsu https://orcid.org/0000-0002-1125-9187
Saurabh W. Jha https://orcid.org/0000-0001-8738-6011
Nathan Smith https://orcid.org/0000-0001-5510-2424
Joshua Haislip https://orcid.org/0000-0002-6703-805X
Vladimir Kouprianov https://orcid.org/0000-0003-3642-5484
Daniel E. Reichart https://orcid.org/0000-0002-5060-3673
Yi Yang https://orcid.org/0000-0002-6535-8500
Jeonghee Rho https://orcid.org/0000-0003-3643-839X

References

Anderson, J. P., Gonzalez-Gaitan, S., Hamuy, M., et al. 2014, ApJ, 786, 67
Andrews, J. E., Pearson, J., Lundquist, M. J., et al. 2022, ApJ, 938, 19
Andrews, J. E., Sand, D. J., Valenti, S., et al. 2019, ApJ, 885, 43
Arnett, W. D. 1982, ApJ, 254, 1
Astropy Collaboration, Price-Whelan, A. M., Sipőcz, B. M., et al. 2018, AJ, 156, 123
Astropy Collaboration, Robitaille, T. P., Tollerud, E. J., et al. 2013, A&A, 558, A33
Becker, A. 2015, HOTPANTS: High Order Transform of PSF ANd Template Subtraction, Astrophysics Source Code Library, ascl:1504.004
Benetti, S., Patat, F., Turatto, M., et al. 1994, A&A, 285, L13
Benetti, S., Turatto, M., Balberg, S., et al. 2001, MNRAS, 322, 361
Bostroem, K. A., Valenti, S., Horesh, A., et al. 2019, MNRAS, 485, 5120
Bostroem, K. A., Valenti, S., Sand, D. J., et al. 2020, ApJ, 895, 31
Brown, P. J., Dessart, L., Holland, S. T., et al. 2007, ApJ, 659, 1488
Brown, T. M., Baliber, N., Bianco, F. B., et al. 2013, PASP, 125, 1031
Bruch, R. J., Gal-Yam, A., Schulze, S., et al. 2021, ApJ, 912, 46
Bullivant, C., Smith, N., Williams, G. G., et al. 2018, MNRAS, 476, 1497
Callis, E., Fraser, M., Pastorello, A., et al. 2021, arXiv:2109.12943
Catchpole, R. M., Menzies, J. W., Monk, A. S., et al. 1987, MNRAS, 229, 15P
Catchpole, R. M., Whitelock, P. A., Feast, M. W., et al. 1988, MNRAS, 231, 75P
Chugai, N. N., Chevalier, R. A., & Utrobin, V. P. 2007, ApJ, 662, 1136
Chugai, N. N., & Utrobin, V. P. 2000, A&A, 354, 557
Corgan, A., Smith, N., Andrews, J., Filippenko, A. V., & Van Dyk, S. D. 2022, MNRAS, 510, 1
Crawford, S. M., Still, M., Schellart, P., et al. 2010, Proc. SPIE, 7737, 773725
Davies, B., & Dessart, L. 2019, MNRAS, 483, 887
Davis, S., Pessi, P. J., Fraser, M., et al. 2021, ApJ, 909, 145
de Jaeger, T., Zheng, W., Stahl, B. E., et al. 2019, MNRAS, 490, 2799
de Vaucouleurs, G., de Vaucouleurs, A., Corwin, H. G. J., et al. 1991, Third Reference Catalogue of Bright Galaxies (New York: Springer)
Dessart, L., Hillier, D. J., Gezari, S., Basa, S., & Matheson, T. 2009, MNRAS, 394, 21
Dessart, L., John Hillier, D., & Audit, E. 2017, A&A, 605, A83
Dong, Y., Valenti, S., Bostroem, K. A., et al. 2021, ApJ, 906, 56
Elmegreen, B. G., Sundin, M., Kaufman, M., Brinks, E., & Elmegreen, D. M. 1995a, ApJ, 453, 139
Elmegreen, D. M., Elmegreen, B. G., Kaufman, M., et al. 2006, ApJ, 642, 158
Elmegreen, D. M., Elmegreen, B. G., Kaufman, M., et al. 2017, ApJ, 841, 43
Elmegreen, D. M., Kaufman, M., Brinks, E., Elmegreen, B. G., & Sundin, M. 1995b, ApJ, 453, 100
Elmegreen, D. M., Kaufman, M., Elmegreen, B. G., et al. 2001, AJ, 121, 182
Faran, T., Poznanski, D., Filippenko, A. V., et al. 2014, MNRAS, 442, 844
Fassia, A., Meikle, W. P. S., Chugai, N., et al. 2001, MNRAS, 325, 907
Fazio, G. G., Hora, J. L., Allen, L. E., et al. 2004, ApJS, 154, 10
Filippenko, A. V. 1997, ARA&A, 35, 309
Filippenko, A. V., Chornock, R., Swift, B., et al. 2003, IAU Circ., 8159, 2
Foreman-Mackey, D. 2016, JOSS, 1, 24
Foreman-Mackey, D., Hogg, D. W., Lang, D., & Goodman, J. 2013, PASP, 125, 306
Förster, F., Moriya, T. J., Maureira, J. C., et al. 2018, NatAs, 2, 808
Fraser, M., Ergon, M., Eldridge, J. J., et al. 2011, MNRAS, 417, 1417
Galbany, L., Hamuy, M., Phillips, M. M., et al. 2016, AJ, 151, 33
Gal-Yam, A., Arcavi, I., Ofek, E. O., et al. 2014, Natur, 509, 471
Gal-Yam, A., Kasliwal, M. M., Arcavi, I., et al. 2011, ApJ, 736, 159
Gehrz, R. D., Roellig, T. L., Werner, M. W., et al. 2007, RScI, 78, 011302
González-Gaitán, S., Tominaga, N., Molina, J., et al. 2015, MNRAS, 451, 2212
Groh, J. H., Meynet, G., Ekström, S., & Georgy, C. 2014, A&A, 564, A30
Gutiérrez, C. P., Anderson, J. P., Hamuy, M., et al. 2017, ApJ, 850, 89
Hamuy, M., & Pinto, P. A. 2002, ApJL, 566, L63
Harris, C. R., Millman, K. J., van der Walt, S. J., et al. 2020, Natur, 585, 357
Hiramatsu, D., Howell, D. A., Moriya, T. J., et al. 2021a, ApJ, 913, 55
Hiramatsu, D., Howell, D. A., Van Dyk, S. D., et al. 2021b, NatAs, 5, 903
Hosseinzadeh, G., & Gomez, S. 2020, Light Curve Fitting, v0.2.0, Zenodo, doi:10.5281/zenodo.4312178
Hosseinzadeh, G., Kilpatrick, C. D., Dong, Y., et al. 2022, ApJ, 935, 31
Hosseinzadeh, G., Valenti, S., McCully, C., et al. 2018, ApJ, 861, 63
Huang, F., Wang, X., Zhang, J., et al. 2015, ApJ, 807, 59
Hunter, J. D. 2007, CSE, 9, 90
Jacobson-Galán, W. V., Dessart, L., Jones, D. O., et al. 2022, ApJ, 924, 15
Jencson, J. E. 2020, PhD thesis, California Institute of Technology
Jencson, J. E., Kasliwal, M. M., Adams, S. M., et al. 2019, ApJ, 886, 40
Jencson, J. E., Kasliwal, M. M., Johansson, J., et al. 2017, ApJ, 837, 167
Jerkstrand, A., Ertl, T., Janka, H. T., et al. 2018, MNRAS, 475, 277
Kasliwal, M. M., Bally, J., Masci, F., et al. 2017, ApJ, 839, 88
Kaufman, M., Elmegreen, B. G., Struck, C., et al. 2016, ApJ, 831, 161
Khazov, D., Yaron, O., Gal-Yam, A., et al. 2016, ApJ, 818, 3
Kirshner, R. P., Arp, H. C., & Dunlap, J. R. 1976, ApJ, 207, 44
Kitaura, F. S., Janka, H. T., & Hillebrandt, W. 2006, A&A, 450, 345
Kozyreva, A., Janka, H.-T., Kresse, D., Taubenberger, S., & Baklanov, P. 2022, MNRAS, 514, 4173
Leonard, D. C., Filippenko, A. V., Barth, A. J., & Matheson, T. 2000, ApJ, 536, 239
Li, W., Van Dyk, S. D., Filippenko, A. V., et al. 2006, ApJ, 641, 1060
Lisakov, S. M., Dessart, L., Hillier, D. J., Waldman, R., & Livne, E. 2017, MNRAS, 466, 34
Lisakov, S. M., Dessart, L., Hillier, D. J., Waldman, R., & Livne, E. 2018, MNRAS, 473, 3863
Lyman, J. D., Levan, A. J., Church, R. P., Davies, M. B., & Tanvir, N. R. 2014, MNRAS, 444, 2157
Maund, J. R., Reilly, E., & Mattila, S. 2014, MNRAS, 438, 938
Maund, J. R., & Smartt, S. J. 2005, MNRAS, 360, 288
Menzies, J. W., Catchpole, R. M., van Vuuren, G., et al. 1987, MNRAS, 227, 39P
Morozova, V., Piro, A. L., Fuller, J., & Van Dyk, S. D. 2020, ApJL, 891, L32
Morozova, V., Piro, A. L., & Valenti, S. 2017, ApJ, 838, 28
Morozova, V., Piro, A. L., & Valenti, S. 2018, ApJ, 858, 15
Munari, U., & Zwitter, T. 1997, A&A, 318, 269
Nakaoka, T., Kawabata, K. S., Maeda, K., et al. 2018, ApJ, 859, 78
Niemela, V. S., Ruiz, M. T., & Phillips, M. M. 1985, ApJ, 289, 52
Nomoto, K. 1984, ApJ, 277, 791
Oke, J. B., Cohen, J. G., Carr, M., et al. 1995, PASP, 107, 375
Pastorello, A., Sauer, D., Taubenberger, S., et al. 2006, MNRAS, 370, 1752
Pastorello, A., Valenti, S., Zampieri, L., et al. 2009, MNRAS, 394, 2266
Pastorello, A., Zampieri, L., Turatto, M., et al. 2004, MNRAS, 347, 74
Pejcha, O., & Prieto, J. L. 2015, ApJ, 806, 225
Phillips, M. M., Simon, J. D., Morrell, N., et al. 2013, ApJ, 779, 38
Pignata, G. 2013, in Massive Stars: From Alpha to Omega, 176
Poelarends, A. J. T., Herwig, F., Langer, N., & Heger, A. 2008, ApJ, 675, 614
Pogge, R. W., McLean, I. S., Ramsay, S. K., et al. 2010, Proc. SPIE, 7735, 77350A
Poznanski, D., Prochaska, J. X., & Bloom, J. S. 2012, MNRAS, 426, 1465
Pumo, M. L., Zampieri, L., Spiro, S., et al. 2017, MNRAS, 464, 3013
Quimby, R. M., Wheeler, J. C., Hoflich, P., et al. 2007, ApJ, 666, 1093
Razza, A., Pineda, J., Gromadzki, M., & Yaron, O. 2018, TNSCR, 2018-2015, 1
Richmond, M. W., Treffers, R. R., Filippenko, A. V., et al. 1994, AJ, 107, 1022
Ricker, G. R., Winn, J. N., Vanderspek, R., et al. 2015, JATIS, 1, 014003
Rubin, A., Gal-Yam, A., De Cia, A., et al. 2016, ApJ, 820, 33
Sand, D. J., Valenti, S., Lundquist, M., Amaro, R., & Wyatt, S. 2018, TNSTR, 2018-2000, 1
Sanders, N. E., Soderberg, A. M., Gezari, S., et al. 2015, ApJ, 799, 208
Sapir, N., & Waxman, E. 2017, ApJ, 838, 130
Schlafly, E. F., & Finkbeiner, D. P. 2011, ApJ, 737, 103
Schlafly, E. F., Finkbeiner, D. P., Schlegel, D. J., et al. 2010, ApJ, 725, 1175
Shivvers, I., Groh, J. H., Mauerhan, J. C., et al. 2015, ApJ, 806, 213
Smartt, S. J., Eldridge, J. J., Crockett, R. M., & Maund, J. R. 2009, MNRAS, 395, 1409
Smartt, S. J., Valenti, S., Fraser, M., et al. 2015, A&A, 579, A40

Smith, M. P., McLean, I. S., Iye, M., et al. 2006, Proc. SPIE, 6269, 62692A
Smith, N. 2014, ARA&A, 52, 487
Smith, N., & Arnett, W. D. 2014, ApJ, 785, 82
Smith, N., Cenko, S. B., Butler, N., et al. 2012, MNRAS, 420, 1135
Smith, N., Mauerhan, J. C., Cenko, S. B., et al. 2015, MNRAS, 449, 1876
Soumagnac, M. T., Ganot, N., Irani, I., et al. 2020, ApJ, 902, 6
Spiro, S., Pastorello, A., Pumo, M. L., et al. 2014, MNRAS, 439, 2873
Springob, C. M., Haynes, M. P., Giovanelli, R., & Kent, B. R. 2005, ApJS, 160, 149
Struck, C., Kaufman, M., Brinks, E., et al. 2005, MNRAS, 364, 69
Suntzeff, N. B., Hamuy, M., Martin, G., Gomez, A., & Gonzalez, R. 1988, AJ, 96, 1864
Szalai, T., Vinkó, J., Könyves-Tóth, R., et al. 2019, ApJ, 876, 19
Takáts, K., Pignata, G., Pumo, M. L., et al. 2015, MNRAS, 450, 3137
Takáts, K., Pumo, M. L., Elias-Rosa, N., et al. 2014, MNRAS, 438, 368
Tartaglia, L., Sand, D. J., Groh, J. H., et al. 2021, ApJ, 907, 52
Tartaglia, L., Sand, D. J., Valenti, S., et al. 2018, ApJ, 853, 62
Terreran, G., Jacobson-Galán, W. V., Groh, J. H., et al. 2022, ApJ, 926, 20
Theureau, G., Hanski, M. O., Coudreau, N., Hallet, N., & Martin, J.-M. 2007, A&A, 465, 71
Tinyanont, S., Ridden-Harper, R., Foley, R. J., et al. 2022, MNRAS, 512, 2777
Tomasella, L., Cappellaro, E., Fraser, M., et al. 2013, MNRAS, 434, 1636
Tsvetkov, D. Y., Shugarov, S. Y., Volkov, I. M., et al. 2018, AstL, 44, 315
Tsvetkov, D. Y., Volnova, A. A., Shulga, A. P., et al. 2006, A&A, 460, 769
Turatto, M., Mazzali, P. A., Young, T. R., et al. 1998, ApJL, 498, L129
Valenti, S., Howell, D. A., Stritzinger, M. D., et al. 2016, MNRAS, 459, 3939
Valenti, S., Sand, D., Pastorello, A., et al. 2014, MNRAS, 438, L101
Valerin, G., Pumo, M. L., Pastorello, A., et al. 2022, MNRAS, 513, 4983
Vallely, P. J., Kochanek, C. S., Stanek, K. Z., Fausnaugh, M., & Shappee, B. J. 2021, MNRAS, 500, 5639
Van Dyk, S., Li, W., & Filippenko, A. 2003, PASP, 115, 1
Van Dyk, S. D., Davidge, T. J., Elias-Rosa, N., et al. 2012, AJ, 143, 19
Virtanen, P., Gommers, R., Oliphant, T. E., et al. 2020, NatMe, 17, 261
Werner, M. W., Roellig, T. L., Low, F. J., et al. 2004, ApJS, 154, 1
Yaron, O., & Gal-Yam, A. 2012, PASP, 124, 668
Yaron, O., Perley, D. A., Gal-Yam, A., et al. 2017, NatPh, 13, 510
Yuan, F., Jerkstrand, A., Valenti, S., et al. 2016, MNRAS, 461, 2003
Zampieri, L., Colpi, M., Shapiro, S. L., & Wasserman, I. 1998, ApJ, 505, 876
Zampieri, L., Pastorello, A., Turatto, M., et al. 2003, MNRAS, 338, 711
Zhang, J., Wang, X., József, V., et al. 2020, MNRAS, 498, 84